Journal of Fluids and Structures (2001) **15,** 791–829
doi:10.1006/jfls.2000.0380, available online at http://www.idealibrary.com on IDEAL®

OSCILLATIONS OF A TURBULENT JET INCIDENT UPON AN EDGE

J.-C. Lin and D. Rockwell

Department of Mechanical Engineering and Mechanics
354 Packard Laboratory, 19 Memorial Drive West
Lehigh University, Bethlehem, PA 18015, U.S.A.

(Received 7 September 1999, and in final form 10 November 2000)

For the case of a jet originating from a fully turbulent channel flow and impinging upon a sharp edge, the possible onset and nature of coherent oscillations has remained unexplored. In this investigation, high-image-density particle image velocimetry and surface pressure measurements are employed to determine the instantaneous, whole-field characteristics of the turbulent jet–edge interaction in relation to the loading of the edge. It is demonstrated that even in the absence of acoustic resonant or fluid–elastic effects, highly coherent, self-sustained oscillations rapidly emerge above the turbulent background. Two clearly identifiable modes of instability are evident. These modes involve large-scale vortices that are phase-locked to the gross undulations of the jet and its interaction with the edge, and small-scale vortices, which are not phase-locked. Time-resolved imaging of instantaneous vorticity and velocity reveals the form, orientation, and strength of the large-scale concentrations of vorticity approaching the edge in relation to rapid agglomeration of small-scale vorticity concentrations. Such vorticity field–edge interactions exhibit rich complexity, relative to the simplified pattern of vortex–edge interaction traditionally employed for the quasi-laminar edgetone. Furthermore, these interactions yield highly nonlinear surface pressure signatures. The origin of this nonlinearity, involving the coexistence of multiple frequency components, is interpreted in terms of large- and small-scale vortices embedded in distributed vorticity layers at the edge. Eruption of the surface boundary layer on the edge due to passage of the large-scale vortex does not occur; rather apparent secondary vorticity concentrations are simply due to distension of the oppositely signed vorticity layer at the tip of the edge. The ensemble-averaged turbulent statistics of the jet quickly take on an identity that is distinct from the statistics of the turbulent boundary layer in the channel. Large increases in Reynolds stress occur due to onset of the small-scale concentrations of vorticity immediately downstream of separation; substantial increases at locations further downstream arise from development of the large-scale vorticity concentrations.

© 2001 Academic Press

1. INTRODUCTION

Impingement of a low Reynolds number planar jet upon an edge is well known to give rise to coherent, self-sustained oscillations. The essential features of jet–edge interaction are generic to a broader range of configurations, including oscillations of an axisymmetric jet impinging upon a plate, oscillations of a shear layer along the mouth of the cavity, and other related systems reviewed by Rockwell & Naudascher (1978, 1979), Rockwell (1983, 1998), Blake & Powell (1986), Crighton (1992) and Howe (1997). Ordered jet–edge oscillations, which have been characterized in various fashions during the past half-century for initially laminar jets, date from the early studies of Brown (1937*a*, *b*), and include those of Nyborg (1954), Powell (1961), Karamcheti *et al.* (1969), Holger *et al.* (1977, 1980), Lepicovsky & Ahuja (1983), as well as experimental and theoretical investigations of the foregoing authors.

0889–9746/01/060791 + 39 $35.00/0 © 2001 Academic Press

Measurement of the magnitude of the force on the edge and the associated sound field were first addressed by Powell (1961). Holger *et al.* (1980) formulated a vortex model for the force, which led to prediction of the sound pressure. Characterization of the flow physics of these initially laminar jet–edge interactions has involved qualitative smoke and dye visualizations, often with pointwise velocity measurements. Karamcheti *et al.* (1969) determined streamwise variations of the velocity fluctuation amplitude and phase along the jet. Kaykayoglu & Rockwell (1986) characterized the detailed distribution of instantaneous pressure along the surface of the edge and demonstrated that the effective location of the force on the edge was not at the tip, but downstream of the tip at a distance corresponding to a significant fraction of the unstable wavelength of the incident jet. Furthermore, the complex, multiple-frequency content of the interaction at the edge is manifested in a corresponding upstream influence, as shown in the experiments of Lucas & Rockwell (1984).

The variation of the dimensionless frequencies of oscillation of laminar jets as a function of impingement distance is summarized by Karamcheti *et al.* (1969), also included in Rockwell & Naudascher (1979), and more recently, by Holger *et al.* (1977), Crighton (1992), and Howe (1997). For all data addressed therein, the conditions at the nozzle exit were laminar. These studies, which represent investigations using both air and water as working fluids, exhibit remarkably similar variations of fL/U with L/H. Distinct stages 1–3 of the oscillation are evident. For a given set of data, it is clear that spectral components corresponding to two simultaneous states of oscillation may occur.

The central elements of the flow physics that give rise to self-sustained oscillations were first put forth by Powell (1961), and they have served as a framework for subsequent investigations, as assessed by Holger *et al.* (1977), Rockwell & Naudascher (1979), Rockwell (1983, 1998), Crighton (1992) and Howe (1997). These elements are, in a general sense: amplification of the disturbance in the jet, giving rise to transverse undulations; interaction of the undulating jet with the leading edge, inducing unsteady loading on the edge; upstream influence from the edge to the sensitive (receptive) region of separation at the jet nozzle exit; and conversion of this upstream influence to an unstable perturbation in the jet shear layer.

Based on extensive studies of nominally laminar jet–edge interactions, cited in the foregoing, it is possible to define a number of unresolved issues, as follows.

(i) Even for the case where the jet is initially laminar, the detailed structure of its oscillation and interaction with the edge are unclarified. All previous related investigations have focused on qualitative flow visualization, along with pointwise measurements of velocity within the undulating jet, force on the edge, and sound pressure away from the edge. Classical flow visualization, e.g., dye and smoke injection and particle streak measurements, can, in many instances, give rise to misinterpretations of the actual, underlying vorticity field, as assessed by Gursul *et al.* (1990) and Gursul & Rockwell (1991). The detailed, quantitative structure of the jet–edge interaction is, of course, crucial for determining the force on the edge, the upstream influence, and the sound pressure.

(ii) The potential for emergence of organized jet oscillations from a fully turbulent channel flow has not yet been explored. In the event that organized oscillations do exist, it is unclear whether a predominant large-scale instability, or both small- and large-scale instabilities, i.e., vortices, occur on a random background. Moreover, the development of patterns of vortical structures upstream of, and immediately adjacent to, the impingement edge is unresolved. The traditional view is that a fully evolved jet vortex street approaches the edge; yet the presence of the edge is expected to continuously influence the vorticity distribution and trajectory of a typical vortex.

(iii) The consequence of the turbulent jet–edge interaction on the surface loading of the edge has not been addressed. In particular, it is unknown whether the spectral content of these surface fluctuations is broad- or narrow band, in the absence of acoustic resonant/fluid–elastic effects. Moreover, both the maximum amplitude and the origin of nonlinearity of the pressure fluctuations on the upper and lower sides of the edge have not been related to the evolution of the instantaneous velocity and vorticity fields.

(iv) The nature of the rapid transformation from the turbulence statistics of the unseparated channel flow to the statistics of the jet is undefined. Furthermore, the character of the turbulence statistics in the tip region of the edge, which is related to the source-like behavior in that region, is unclarified.

The present investigation addresses these issues using a global technique to determine the instantaneous structure of the jet, in relation to measurement of the surface loading on the edge.

2. EXPERIMENTAL SYSTEM AND TECHNIQUES

Experiments, which were performed using a large-scale jet–edge apparatus housed within a water channel system, involved particle image velocimetry, in conjunction with pointwise surface pressure measurements. The experimental system and techniques are described in the following.

2.1. Experimental System

A large-scale water channel housed the jet–edge system. The water channel has a test-section 610 mm wide × 610 mm deep, and a length of 4 572 mm. This main test-section is preceded by a contraction having an inlet width of 18 289 mm; the corresponding contraction ratio is therefore 3:1. A honeycomb-screen system is located at the inlet of the contraction, in order to minimize the free-stream turbulence, which is typically less than 0·1%.

2.1.1. *Inlet contraction*

The jet–edge test-section was located within the water channel test-section in the manner indicated in Figure 1. Its overall length was 6 553 mm. The principal components are an inlet contraction, a flow development channel, the edge system and the outflow section. As illustrated in the plan view of Figure 1, the deployment of two flow barriers, on either side of the test-section, precluded flow through the gap between the jet–edge test-section and the water channel test-section. In essence, this barrier system created a large reservoir of very low velocity water, which was drawn into the inlet contraction, in the manner depicted by the pattern of arrows in the plan view. Inclusion of a honeycomb at the upstream end of the inlet contraction provided a significant pressure drop, and ensured that the flow entering the inlet contraction was essentially uniform, except for viscous layers adjacent to the wall of the jet–edge test section. The contraction ratio of the inlet contraction was 20:1.

2.1.2. *Flow development channel*

In order to ensure that a fully developed turbulent boundary layer was attained, a flow development channel, having a width of 3 175 mm and a height $2H = 25{\cdot}4$ mm, was specified. This corresponds to a channel length-to-height ratio of 125:1 and

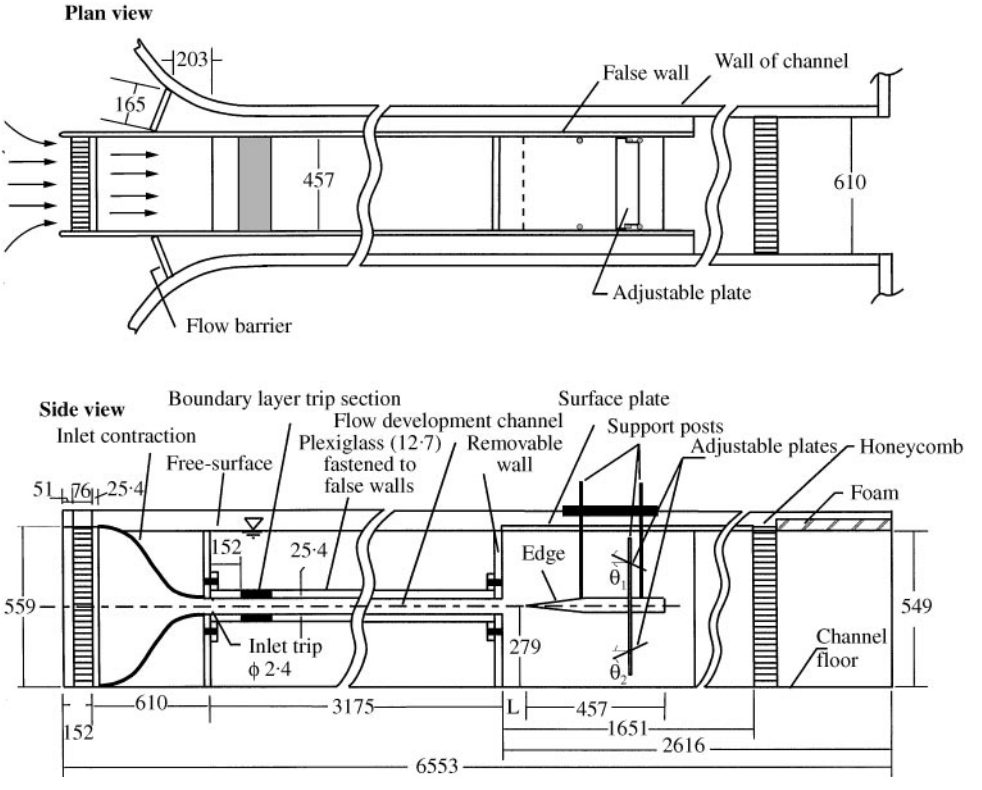

Figure 1. Overview of jet–edge system.

a span-to-height ratio of 18:1 determined from the summary of Niederschulte (1989) on conditions for attainment of fully developed channel flows.

In order to abruptly trip the boundary layer at the inlet to the flow development channel, two brass rods of diameter 2·4 mm were affixed to the bottom and top walls of the channel, at a location immediately downstream of the channel inlet. This trip is similar in concept to that employed by Niederschulte (1989), and promotes the rapid onset of transition. In addition, a special boundary layer trip section was employed in the present channel. It consisted of a pattern of hemispheres of varying diameter, mounted on both the bottom and top walls of the channel. The length of this boundary layer trip section was 203 mm. Its leading-edge was located at a distance of 152 mm downstream of the channel inlet. Extensive dye visualization showed that the combination of the inlet trip cylinders and the boundary layer trip section promoted very rapid onset of a turbulent channel flow. Full details of this trip section are described by Johansson & Smith (1983) and Rockwell & Lin (1996).

2.1.3. *Jet–edge system*

The edge system, indicated in Figure 1, involved a sharp leading-edge made of Plexiglas; details are described subsequently. The edge was suspended by four support posts, in the

form of brass rods of 12·7 mm diameter. These four rods connected the Plexiglas edge to a Plexiglas plate located outside the test-section. The junction of the rod with the plate was stabilized via a flange welded to the rod. This support system for the edge ensured that edge vibrations did not occur. It also allowed vertical adjustment of the edge, in order to ensure symmetry of the jet–edge encounter as well as translation of the edge along the test-section, thereby providing variation of impingement distance L. In order to fine-tune the symmetry of the flow along the lower and upper sides of the edge, an adjustable plate system was incorporated. The length of each of these adjustable plates was 457 mm. The plate angles, θ_1 and θ_2, could be altered. During the course of the experiment, their nominal values were $31{\cdot}5^\circ \leq \theta \leq 41^\circ$. In the absence of these adjustable plates, large-scale, very low velocity recirculation zones could build up at that location of the test-section, and bias the jet–edge interaction to an asymmetrical state. During all experiments, the jet–edge interaction was continuously visualized using dye and laser sheet visualization. Moreover, the upper and lower instantaneous surface pressures on the edge were continuously monitored. Both of these criteria were effective in ensuring that the jet–edge encounter was essentially a symmetrical one during the course of all experiments.

Of particular importance is the inclusion of a surface plate, which was in contact with the free-surface, and prevented undesirable generation of free-surface perturbations. In fact, in the absence of the surface plate, substantial free-surface standing wave modes could be induced; they contaminated the fundamental hydrodynamics of the jet–edge interaction. This surface plate extended well downstream of the jet–edge arrangement, as illustrated in Figure 1.

2.1.4. *Outflow section*

Resistance between the jet–edge section and the main exhaust reservoir of the water channel system was provided by the honeycomb arrangement shown in Figure 1. A surface plate, which prevented contamination by oscillations of the free-surface, extended from the channel exit to the location of the honeycomb. Downstream of the honeycomb, porous foam was placed in contact with the free-surface. This foam arrangement extended to the inlet of the exhaust reservoir. The foam further ensured damping of perturbations induced by the organized jet–edge oscillations.

2.1.5. *Impingement edge*

The impingement edge, which is illustrated in Figure 1, was made entirely of Plexiglas. It had an included angle of 19°, a thickness of 18 mm, and a span of 457 mm, thereby extending across the entire test-section. Pressure taps of diameter 0·726 mm were located at a distance of 7·62 mm downstream of the tip of the edge. One tap was located on the top surface and another on the bottom surface. The taps were at the same spanwise location. These lines, which were actually small milled channels having a square cross-section of 1·5 mm × 1·5 mm, terminated in the transducer box, that housed the two high-sensitivity pressure transducers. Two PCB Model No. 106B50 pressure transducers were employed. They were custom-manufactured for long-term immersion in water. The natural frequency of the transmission line-cavity-pressure transducer system was determined, by transient testing, to be 30·5 Hz, which is a factor of approximately 15 higher than the predominant frequency of the jet–edge oscillation. Evaluation of the damping coefficient during the transient response experiments indicated that the maximum distortions of the pressure magnitude and phase were within 0·5%.

2.2. Experimental Techniques

2.2.1. *High-image-density PIV technique*

A laser-scanning version of high-image-density PIV, described in detail by Rockwell *et al.* (1993), was employed in the present experiments. Illumination was provided by a laser, of the continuous wave Argon-ion type. It had a maximum output of 25 W. In essence, a scanning laser sheet was generated by impingement of the focused laser beam on a rotating polygon mirror. Details of the optical arrangement are described in the following.

This laser beam was transmitted through a laser-optical arrangement, which was mounted on a rail system. The optics could therefore be translated along the streamwise direction. Moreover, an additional rail allowed translation in the cross-stream direction. A beam-steering mirror and convex and concave lenses, having focal lengths $f = 300$ and 100 mm, respectively were fixed to the translating table. The multi-faceted rotating mirror, from which the incident beam was reflected to produce a scanning sheet, along with a focusing singlet and a second beam steering mirror, were mounted on a circular table, which could be rotated to any angular position. This optical system allowed the laser beam to be focused to a sufficiently narrow waist, to provide a beam diameter in the measurement region of interest of approximately 1 mm.

The rotating mirror had 48 facets. The effective scanning rate of the laser beam was accomplished by controlling its speed of rotation. The scanning frequency was 624 cycles/s for imaging of the jet–edge flow and 1 529 cycles/s for imaging of the channel flow. Proper selection of this frequency is critical, in order to optimize the displacement between the multiply exposed images of particles, which had a diameter of 12 μm.

A Nikon F-4 camera with a motor drive was employed to obtain still photos of the turbulent channel flow and the jet–edge oscillation. For the purposes of these experiments, corresponding to randomly acquired images, the camera was triggered externally and the motor-driven capability of the camera was not employed. High-resolution 35 mm film with an effective resolution of 300 lines/mm was used. A second camera system, a Hulcher cinema camera, was employed for image acquisition highly resolved in time. This image sequence is referred to hereafter as the highly resolved cinema sequence, corresponding to a maximum framing rate of 40 frames/s. Images were recorded on 100 foot spools of 35 mm film. Finally, for a cinema sequence of lower time resolution, extending over a number of cycles of the jet–edge oscillation, a motor-driven Canon camera was employed; it had a maximum framing rate of 9 frames/s. During both types of cinema image acquisition, the pressure signals at the lower and upper taps along the surface of the edge were acquired simultaneously. This approach allowed a direct correlation between the induced surface pressure and the dynamics of the unsteady, impinging jet. Details of these cinema techniques, involving synchronization of the framing camera with the components of the image and data acquisition systems, as well as representative images, are given by Lin & Rockwell (1998).

Proper selection of the magnification factors of the lenses on the Nikon F-4, Hulcher and Canon cameras was critical, since the magnification factor is, in the end, related to the effective grid size of the pattern of velocity vectors. For the case of the turbulent channel flow, for which only the Nikon F-4 camera was employed, the magnification was 1 : 1·17. It provided a sufficiently small grid size such that a total of 60 data points could be attained across the 25·4 mm channel flow. For photographing the jet–edge oscillations, using the Nikon F-4, Hulcher, and Canon cameras, magnifications M in the range $1{:}5{\cdot}45 \leq M \leq 1{:}5{\cdot}78$ were employed.

Implementation of all camera systems required a means of precluding directional ambiguity of the acquired particle images. An oscillating bias mirror, i.e., an image shifting mirror, was located in front of the camera lens of both the Nikon F-4 and the Hulcher cinema cameras. The angular displacement of the mirror was triggered during each shutter opening, thereby imparting a constant bias displacement of all particle images recorded on the film. This bias was then removed during the interrogation process. The angular displacement of the mirror was of the order of 0·01°, in order to avoid any type of systematic distortion of the recorded pattern of particle images, which would be present for a finite rotation angle of the mirror.

A Nikon digitizing system allowed each 35 mm negative to be digitized at a relatively high resolution of 125 pixels/mm. Subsequently, these patterns of digitized images were evaluated using a single-frame, cross-correlation technique. This approach provided an instantaneous velocity vector at each interrogation location. A standard, 50% overlap of the interrogation areas was employed. For the channel flow, the effective grid size, in the plane of the laser sheet, i.e., the distance between velocity vectors, was 0·42 mm. For the case of the jet–edge images, obtained with the Nikon F-4, Hulcher and Canon cameras, the effective grid sizes Δ were in the range $1{\cdot}82 \leq \Delta \leq 2{\cdot}08$ mm.

After post-processing of the raw velocity field, spurious (outlying) vectors were removed, then blank regions were filled using an established bilinear interpolation technique. The number of spurious vectors in the flow field never exceeded 0·5% of the total vectors. A Gaussian filter, with an exponent $p = 1{\cdot}3$, was employed to smooth the velocity field, without inducing a significant distortion over the scales of interest in the present study. Landreth & Adrian (1990) provide an assessment of these interpolation and filtering techniques.

Two image areas were employed for acquisition of PIV images of the approach turbulent channel flow and the jet–edge oscillation. They are defined with respect to an (x, y) coordinate system, having its origin on the centerline and at the exit of the channel. The image area employed for characterizing the turbulent channel flow had an aspect ratio of approximately 1·5:1. Its left and right boundaries were located at distances $x = -172$ and -132 mm, respectively. The image area used for the overview of the jet–edge oscillations also had an aspect ratio of approximately 1·5:1. This view was employed for the randomly acquired sequence of images, and the cinema sequences with high and low time resolution. For these three experiments, the average locations of the left and right boundaries were, respectively: $x = -2{\cdot}2$ mm, 174·1 mm; $x = -2{\cdot}3$ mm, 168·2 mm; and $x = -3{\cdot}6$ mm, 172·6 mm.

2.2.2. *Pressure measurements*

The time histories of the pressure and velocity fluctuations were acquired at critical locations specified with respect to the aforementioned coordinate system. Appropriate analog filtering and amplification were employed. The sampling time allowed resolution of all dominant frequency components, up to the fourth harmonic of the fluctuation induced by the jet–edge oscillation. Signals were transmitted through the A/D board of the host microcomputer. The nondimensional frequency spectrum was computed using an FFT technique. The total acquisition time of each velocity and pressure record corresponded to, for example, 256 cycles of the predominant jet–edge oscillation at 1·26 Hz. The values of effective sampling time Δt and sampling frequency Δf are indicated in the figures corresponding to each of the time traces and spectra. Filtering using two analog filters, one for each of the pressure transducers, was done in the low-pass mode, with a cut-off frequency of 10 Hz.

3. TURBULENT CHANNEL FLOW

The fully developed turbulent channel flow was characterized by acquisition of images at the location upstream of the channel exit defined in Section 2. In a typical image, approximately 5 800 velocity vectors were obtained. Representative instantaneous velocity fields are given for two different reference frames in Figure 2(a).

To determine the time-averaged statistics of the turbulent channel flow, a total of 20 PIV images were acquired at random times. The minimum time spacing was 10 s, much longer than the estimated time scale of the largest eddy in the channel flow, i.e., of the order of 0·066 s. For evaluation of all averaged and statistical quantities, the variation of the velocity with coordinate x was considered at a given value of y in a specified image. This provided, for a given image, values of mean velocity components $\bar{u}$ and $\bar{v}$, the corresponding r.m.s. values u_{rms} and v_{rms}, as well as the velocity correlation $\overline{u'v'}$. Then, by averaging these values obtained from all images, final statistics were obtained. This approach is the same as that employed by Liu *et al.* (1991) and Rockwell & Lin (1996).

Extensive consideration was given to the detailed LDA measurements of Niederschulte (1989), which extended over the range of Reynolds number $2\,457 \leq \mathrm{Re} \leq 18\,339$ based on half-channel width. For the present experiments, the corresponding value was $\mathrm{Re} = 5\,472$, and the closest value of Niederschulte (1989) is $\mathrm{Re} = 2\,777$; therefore, comparisons were made at $\mathrm{Re} = 2\,777$. It should also be noted that Liu *et al.* (1991) have carried out a high-resolution PIV study of the same channel flow as Niederschulte (1989). Their data agree closely with those of Niederschulte (1989), and therefore are not repeated here. Finally, we note that Kim *et al.* (1987) have performed a direct numerical simulation of the turbulent statistics of a fully developed in channel flow. The Reynolds number of their DNS calculations corresponds to $\mathrm{Re} = 2\,800$. These calculation results were also used as a basis for comparison.

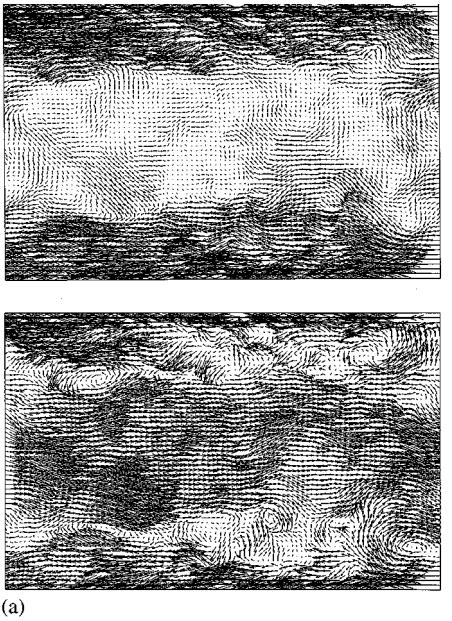

(a)

Figure 2(a). Instantaneous velocity fields of turbulent channel flow shown in reference frames moving with the maximum velocity $\bar{U}_m$ (top image) and spatially averaged velocity $\bar{U}_M$ (bottom image).

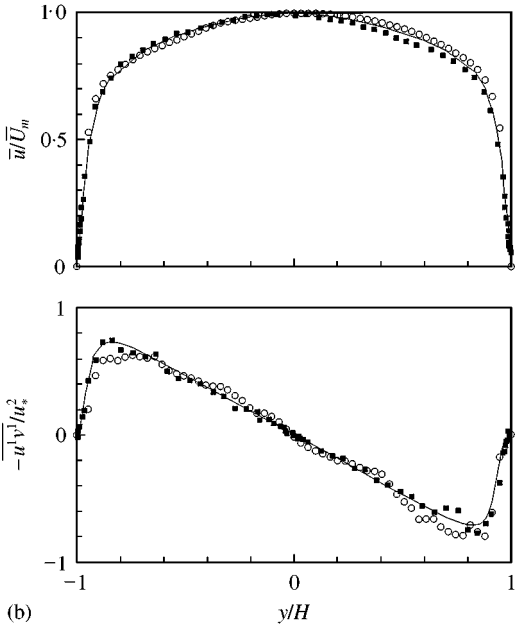

Figure 2(b). Variation of mean velocity distribution across the channel (top plot) and Reynolds stress normalized by friction velocity (bottom plot). The present PIV measurements are compared with LDA measurements of Niederschulte (1989) and direct numerical simulation (DNS) of Kim et al. (1987): ○, Present [PIV]; ■, Niederschulte (1989) [LDA]; ——, Kim *et al.* (1987) [DNS].

The top plot of Figure 2(b) shows a direct comparison of the time-averaged velocity $\bar{u}$ normalized with respect to the maximum velocity $\bar{U}_m$ at the center of the channel. This comparison includes: the present investigation; the LDA data of Niederschulte (1989); and the DNS simulation of Kim *et al.* (1987). The bottom plot of Figure 2(b) shows the velocity correlation component of the Reynolds stress, i.e., $\overline{u'v'}$, normalized with respect to the square of the wall friction velocity $u_* = 17{\cdot}5$ mm/s. In both plots, the agreement is acceptable in view of the difference in Reynolds number and the limited number of images employed in the averaging.

Further evaluation of the images provided distributions of u_{rms}/u_* and v_{rms}/u_* across the channel. Moreover, in order to confirm the existence of a well-defined log layer, data were evaluated to demonstrate the existence of a logarithmic region extending from approximately $y^+ = 20$ to 150. Finally, verification of an inertial subrange within the turbulent channel flow was accomplished by undertaking a spectral analysis based on the PIV images. The classical $n = -5/3$ slope was evident over a substantial range of dimensionless frequency fH/u_*. Detailed distributions are given by Rockwell & Lin (1997).

4. JET–EDGE OSCILLATIONS: SURFACE PRESSURE FLUCTUATIONS

The time history of the jet–edge interaction was characterized using a variety of pointwise pressure and velocity measurements, as described by Rockwell & Lin (1997). Preliminary experiments to determine the principal oscillation characteristics were carried out by varying the impingement length L. Then, the optimum value of L was determined after

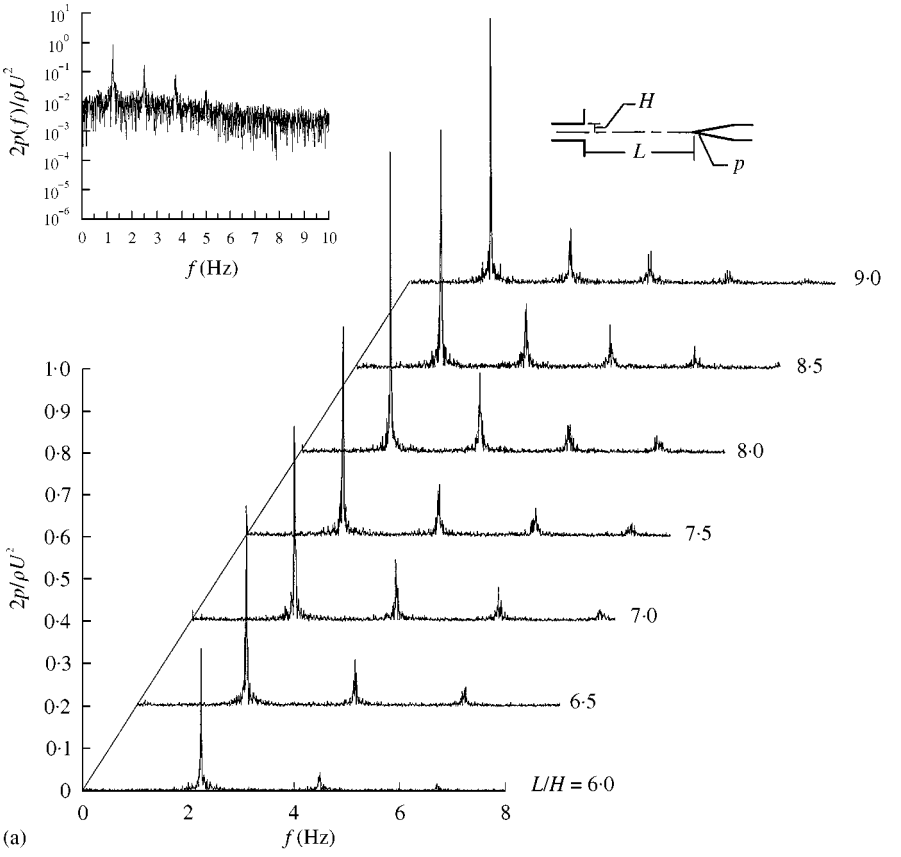

Figure 3(a). Spectra of pressure fluctuation on lower surface of impingement edge as a function of dimensionless impingement distance. The inset shows a typical spectrum plotted on a logarithmic scale.

considering the strength of the pressure fluctuations, in conjunction with optimization of the field of view and magnification factor of the PIV measurements. The value of dimensionless impingement length eventually chosen corresponds to $L/H = 10$, in which H is the channel half-width.

Pressure spectra were acquired at a relatively large number of values of L/H; only selected spectra are exhibited in Figure 3(a) and 3(b). The plot at the upper left of Figure 3(a) gives the spectral amplitude plotted on logarithmic coordinates. It shows the degree of predominance of the organized components relative to the background. The fundamental component at $f = 1{\cdot}35$ Hz extends about one and one-half decades above the background. Well-defined peaks up to the fourth harmonic are evident. In addition, rather broadly distributed peaks are evident between these higher harmonics, and a broadly distributed subharmonic of the fundamental, occurring at approximately $f = 0{\cdot}61$ Hz, is apparent.

Extensive diagnostic experiments were conducted in order to determine the variation of the predominant spectral components over a range of L/H extending from approximately the onset of the self-excited oscillation to attainment of its maximum amplitude. These spectra are shown for extreme values of L/H in Figure 3(a) and 3(b). All spectra exhibit predominance of the fundamental component, whose frequency decreases with increasing L/H, and at least at two or three higher harmonics.

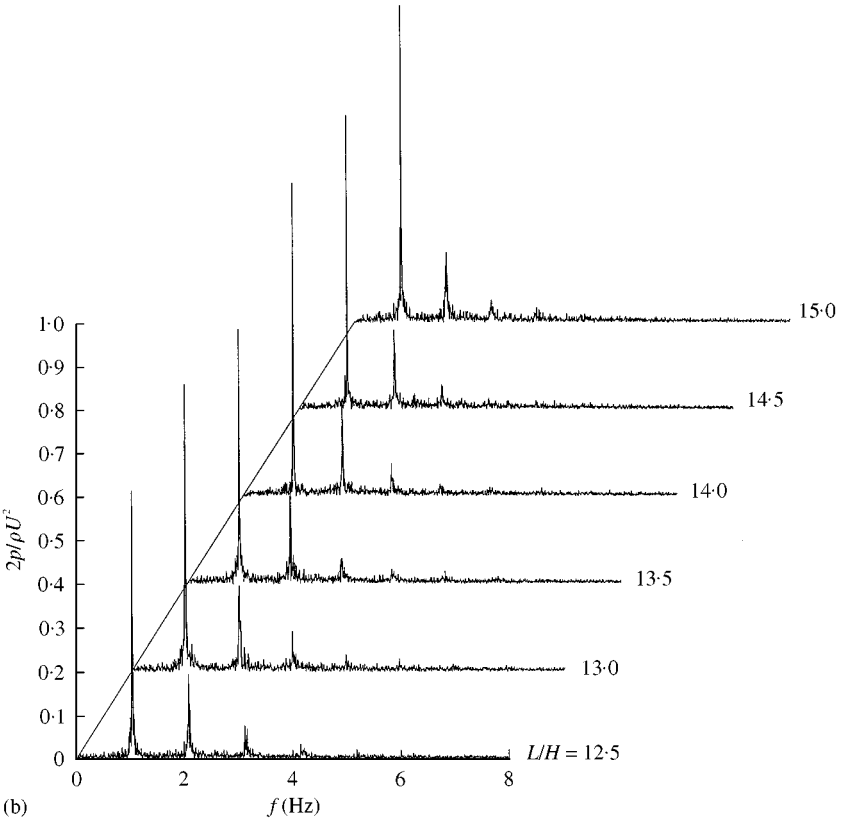

Figure 3(b). Spectra of pressure fluctuation on the lower surface of the impingement edge as a function of dimensionless impingement distance.

Examination of the spectra of the peaks of the fundamental component in the spectra of Figure 3(a) and 3(b), with variations in impingement length L/H, reveals the following characteristics: onset of pronounced jet–edge oscillations at $L/H = 6{\cdot}0$ (below this value of L/H, sharply defined peaks were not detectable in the pressure spectra); a rapid increase in amplitude from $L/H = 6{\cdot}0$ to $11{\cdot}0$ (not shown herein); attainment of maximum amplitude at $L/H = 11{\cdot}0$ (not shown), followed by generally decreasing amplitude at larger values of L/H; and, finally, occurrence of predominant oscillations only in the fundamental mode over the entire range of impingement length L/H up to $15{\cdot}0$. These trends are in remarkable accord with the measured variation of the total force F as a function of impingement length L/H measured by Powell (1961) for a low Reynolds number jet at $\mathrm{Re} = 346$.

The frequencies of each of the discernible spectral components in Figure 3(a) and 3(b), as well as components at intermediate values of L/H, were evaluated and plotted as dimensionless frequency fL/U as a function of L/H. The result is shown in Figure 4. The present data are compared with low Reynolds number, quasi-laminar air and water jets impinging upon an edge. Whereas the fundamental component $k = 1$ of the present study, occurring at approximately $fL/U = 0{\cdot}5$ lines up well with the first stage $n = 1$ of the classical laminar jet oscillation, the higher harmonic components $k = 2{,}3$ of the present study are not coincident with the second and third stages $n = 2{,}3$ of the laminar jet oscillation. This suggests that, in the present case of turbulent jet–edge interaction, the higher modes are due to strong

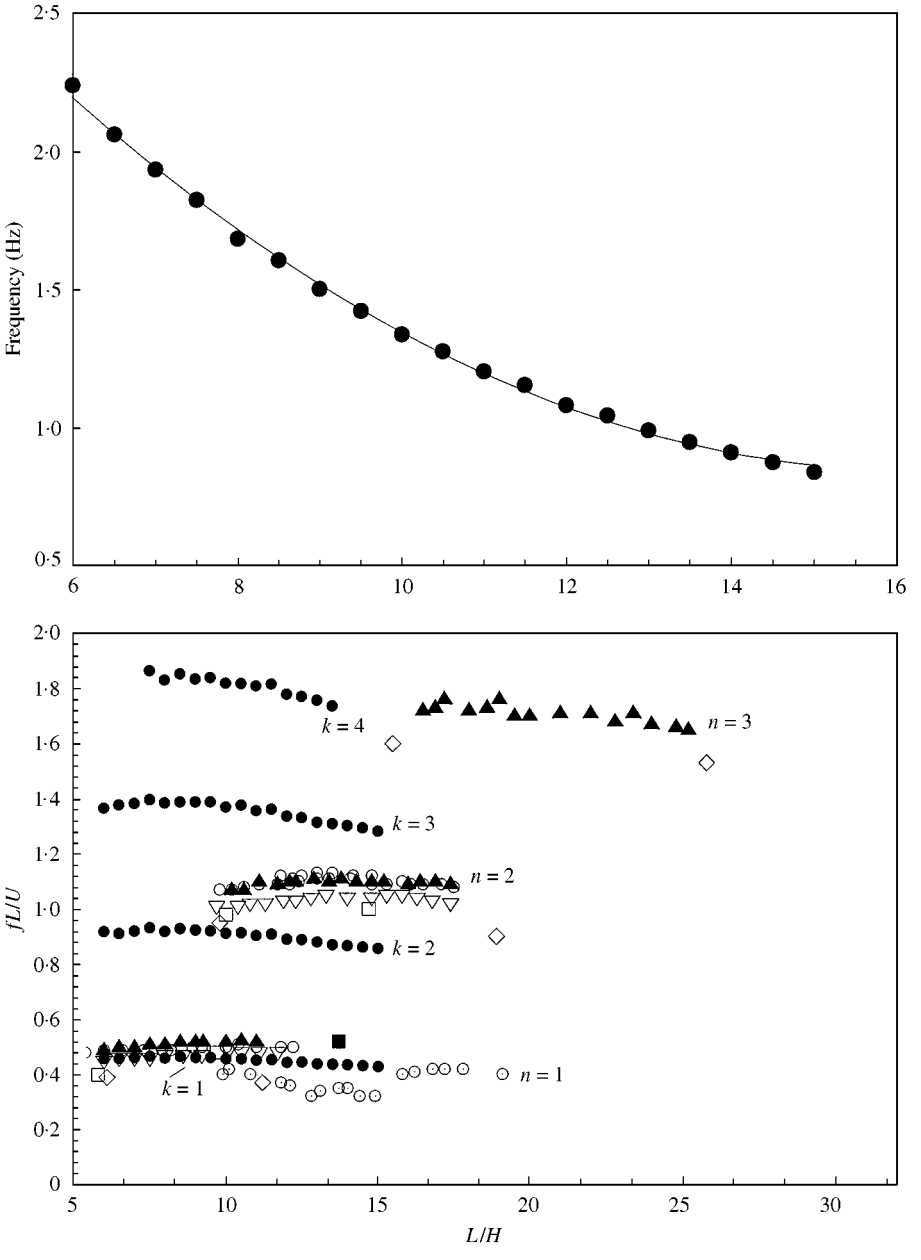

Figure 4. Comparison of variations of dimensionless frequency with dimensionless impingement distance for the present and previous investigations. For the present study of an initially turbulent jet, all four detectable spectral peaks $k = 1, 2, 3$, and 4 are represented. Previous studies, which typically exhibit modes $n = 1, 2$, and 3, involve laminar jet formation from the nozzle exit. ●, Present; ◇, Brown; ■, Nyborg; □, Powell; ▲ ▽ ○ ⊙, Karamcheti; *et al.*; ▲, (Round edge); ▽, (30° edge).

nonlinearity of the jet–edge oscillation. On the other hand, for the laminar jet, the basic pattern of the local jet–edge interaction region undergoes fundamental alterations with increasing stage number (Brown 1937*a*, *b*; Lucas & Rockwell 1984).

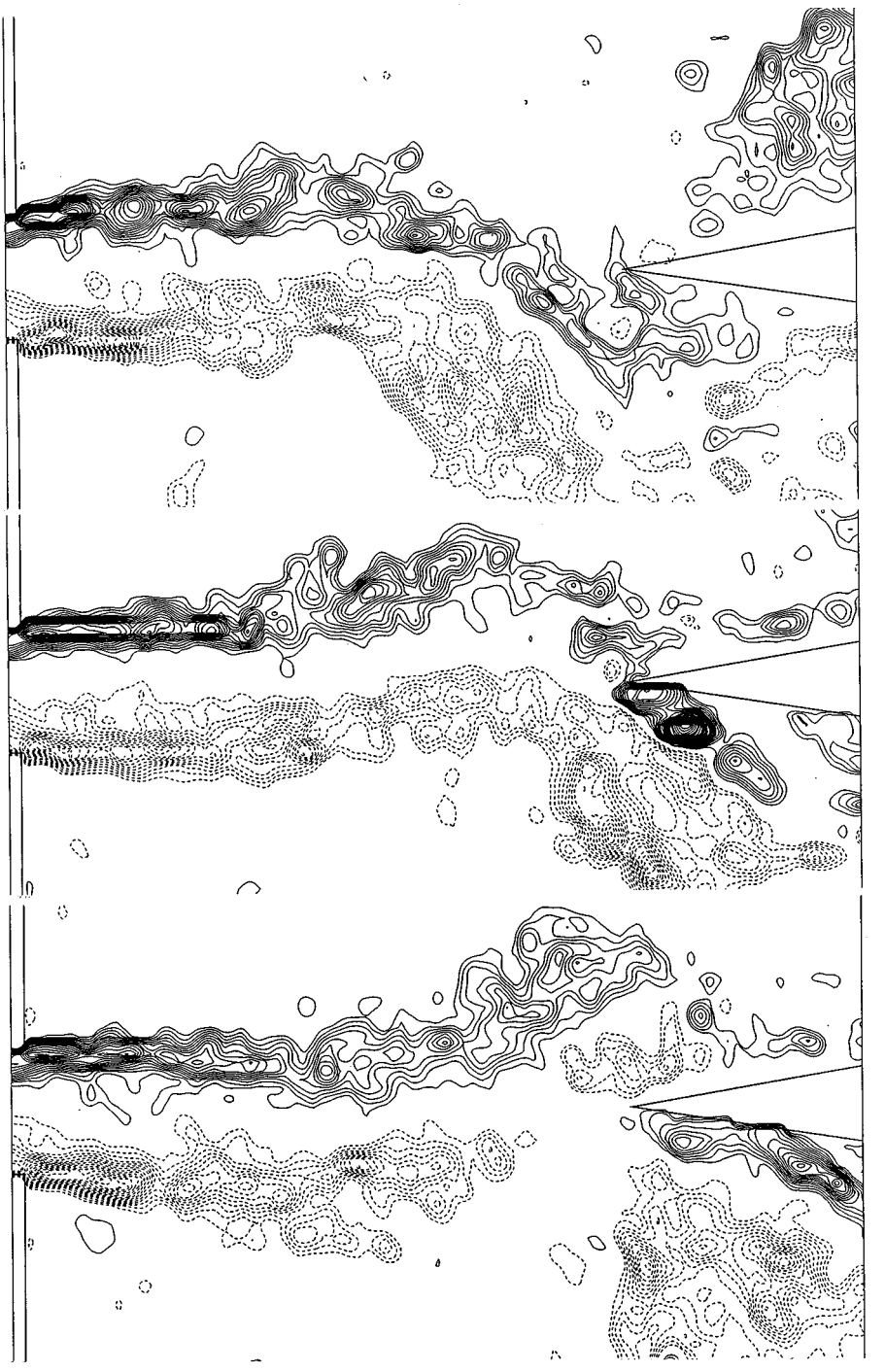

Figure 5. Comparison of vorticity distributions at three successive phases of the jet oscillation. Images are from a randomly acquired series. Minimum vorticity $\omega_{\min} = \pm 10$; incremental vorticity $\Delta\omega = 5\ \mathrm{s}^{-1}$.

5. JET–EDGE OSCILLATIONS: INSTANTANEOUS STRUCTURE

5.1. Randomly Acquired Images

Thirty-six images were randomly acquired over a long time span. The minimum time between two consecutive images was > 10 s, which is at least a factor of 10 longer than the shortest period of the predominant (fundamental) component of the self-sustained jet–edge oscillation. In the following, the instantaneous images of vorticity and velocity in different reference frames provide insight into the instantaneous structure of the jet–edge interaction that, in turn, allows physical interpretation of the time-averaged statistics addressed in Section 6.

Examination of the entire sequence of 36 randomly acquired images shows that essential features of the time-dependent oscillation could be reconstructed using a limited number of images. This is possible due to the highly coherent oscillations at the predominant (fundamental) component, already evident in the pressure spectra of Figures 3(a) and 3(b). Figure 5

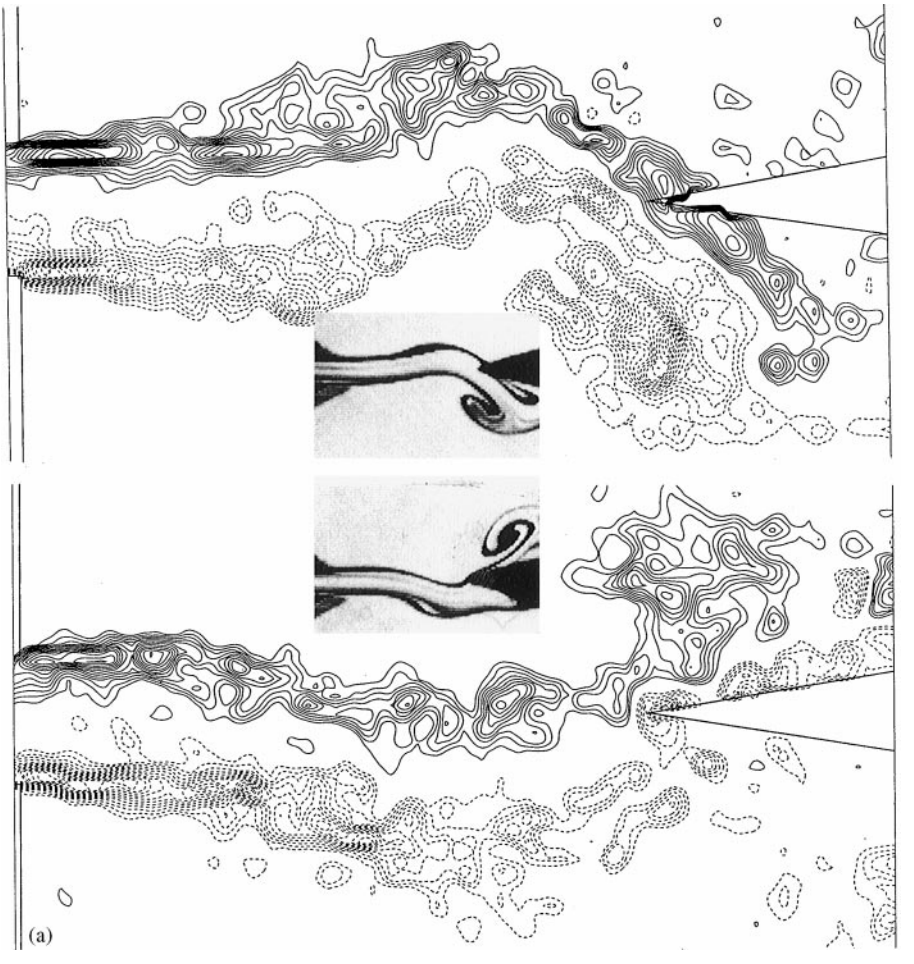

Figure 6(a). Comparison of instantaneous distributions of vorticity with the qualitative dye visualization of Lucas & Rockwell (1984) for the case of an initially laminar jet at Re = 300. $\omega_{\min} = \pm 10\ s^{-1}$. $\Delta\omega = 5\ s^{-1}$.

shows such a reconstruction corresponding to three successive instants. First of all, tracking the large-scale cluster of negative vorticity in the lower part of the image, it moves downstream beneath the edge with increasing time. Correspondingly, the positive layer of vorticity is deflected upward and simultaneously undergoes coalescence of positive vorticity into the initial stages of a large-scale cluster, which eventually will take the mirror image form of the large-scale negative cluster. This positive layer of vorticity is severed at the tip of the edge, particularly evident in the middle image. After this severing occurs, the layer of positive vorticity moves downstream along the lower surface of the impingement edge. An inherent feature of both the positive and negative vorticity layers is the rapid onset of small-scale vortical structures immediately downstream of the nozzle exit. They are addressed in detail subsequently.

Comparison of the overall, global structure of the initially turbulent jet with the low Reynolds number (laminar) jet of Lucas & Rockwell (1984) is given in Figure 6(a). The dye visualization image shown superposed on the corresponding PIV images taken at the same phase of the jet oscillation cycle exhibits a remarkable similarity to the overall global characteristics of the instantaneous PIV images. For example, the top dye image indicates: formation of a large-scale vortex, which is approximately centered at the tip of the edge; severing of the upper layer of the jet by the tip of the edge; and upward deflection of the jet centerline immediately upstream of the tip of the edge. All of these features are evident in the PIV image. Corresponding global similarities are evident in the low Reynolds number dye photo and high Reynolds number PIV image shown at the bottom of Figure 6(a).

Figure 6(b) shows remarkable similarity between the low Reynolds number air jet of Brown (1937*a*, *b*) and the instantaneous PIV image: formation of an elongated, large-scale concentration of vorticity in the upper layer of the jet, at a location upstream of the tip; upward deflection of the jet centerline in that region; and formation of a large-scale vortex of opposite sense centered immediately downstream of the tip. These global features exhibit similar features despite the differences in working fluid and initial conditions of the jet.

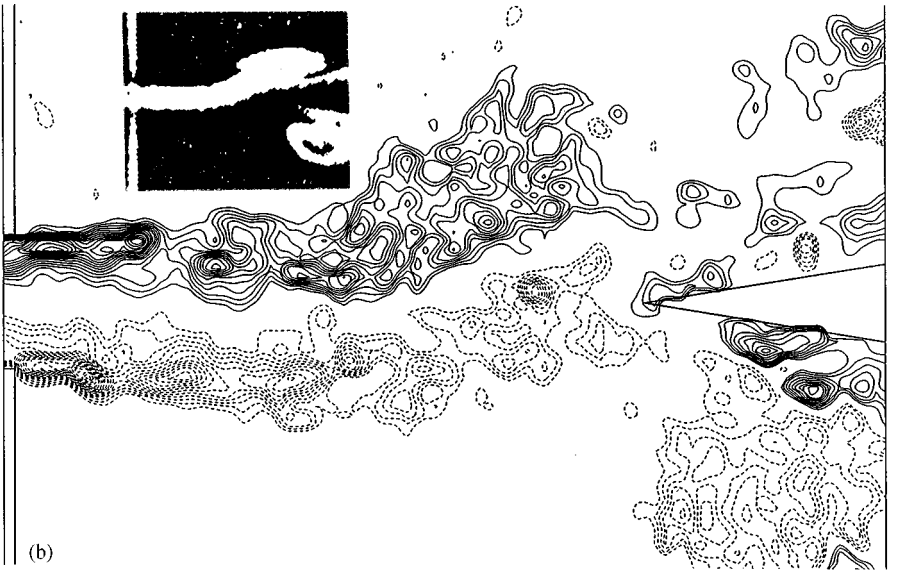

Figure 6(b). Comparison of instantaneous distribution of vorticity with the qualitative smoke visualization of Brown (1937) at a value of Reynolds number Re = 183. Minimum vorticity level $\omega_{\min} = \pm 10\,\mathrm{s}^{-1}$ and $\Delta\omega = 5\,\mathrm{s}^{-1}$.

5.2. Cinema Acquisition of Images

Cinema sequences were acquired using two different cameras and nominal framing rates. For the first cinema sequence yielding a highly time-resolved series of images, the Hulcher camera operating at 40 frames/s was employed. The intent of this series is to show the evolution of both the small- and large-scale vortical structures, in relation to the variation of the instantaneous pressure traces along the upper and lower surfaces of the impingement edge. For the second cinema sequence, the intent was to generate a phase-referenced series of images; the motor-driven Canon camera was employed at a framing rate of 8·8 frames/s. These images, acquired over approximately five cycles of the jet oscillation, allow characterization of the degree to which time evolution of the vortical structures in the jet is repetitive from cycle to cycle.

5.2.1. *Highly time-resolved cinema sequence*

First, representative features of the jet–edge interaction are described at crucial instants during the oscillation cycle. Figure 7 shows the pressure trace acquired during the cinema sequence; the dots indicate the instants at which three representative images were processed, in order to show transformation from the minimum to maximum values of the pressure p_u on the upper surface of the edge and simultaneously from the maximum to minimum of pressure p_l on the lower surface of the edge. The spectra corresponding to these two traces are indicated at the bottom of Figure 7. Due to the substantial nonlinearity of these pressure traces, the middle point on the upper trace p_u does not lie midway between the points of minimum and maximum amplitude. On the other hand, for the pressure signal p_l acquired along the lower surface, the three points are approximately equally spaced.

Instantaneous images at these three instants are shown in Figure 8(a)–8(c). In each figure, the uppermost image corresponds to contours of constant vorticity, the middle image to the velocity field measured in the laboratory frame, and the bottom image to the velocity field viewed in the reference frame moving at $\sim 0{\cdot}5\bar{U}_m$, where $\bar{U}_m$ is the maximum (centerline) velocity at the exit of the channel. In Figure 8(a), the pressure on the upper surface of the edge is maximum-negative, and that on the bottom surface is maximum-positive. At this instant, the upper image showing the patterns of vorticity reveals that the large-scale concentration of positive (solid line) vorticity has just passed over the pressure tap on the upper surface of the edge. Correspondingly, a moderate-scale positive concentration of vorticity is located immediately upstream of the tip of the edge. The pattern of velocity vectors shown in the middle image clearly indicates the downward deflection of the jet in the vicinity of the leading-edge, and the occurrence of a large-scale swirl pattern above the edge, due to the large-scale concentration of vorticity. In the bottom image, representing the velocity field in the moving reference frame, the velocity vectors are directed towards the surface of the edge at the location of the lower pressure tap and generally away from the edge at the location of the upper tap. Moreover, the large-scale swirl pattern of velocity vectors is again clearly evident.

For the next instant, represented in Figure 8(b), the pressure on the upper surface is nearly at its maximum-positive value, while that on the lower surface is approximately zero. The pattern of vorticity concentrations indicates that the moderate-scale cluster of positive (solid line) vorticity collides with the edge and, in fact, appears to be severed in the region of the tip of the edge. At this instant, the large-scale negative concentration of vorticity is nearly centered beneath the lower pressure tap. The corresponding velocity field in the laboratory frame, shown in the middle image, indicates the severe upward deflection of the jet immediately upstream of the leading edge, and downward deflection in the region

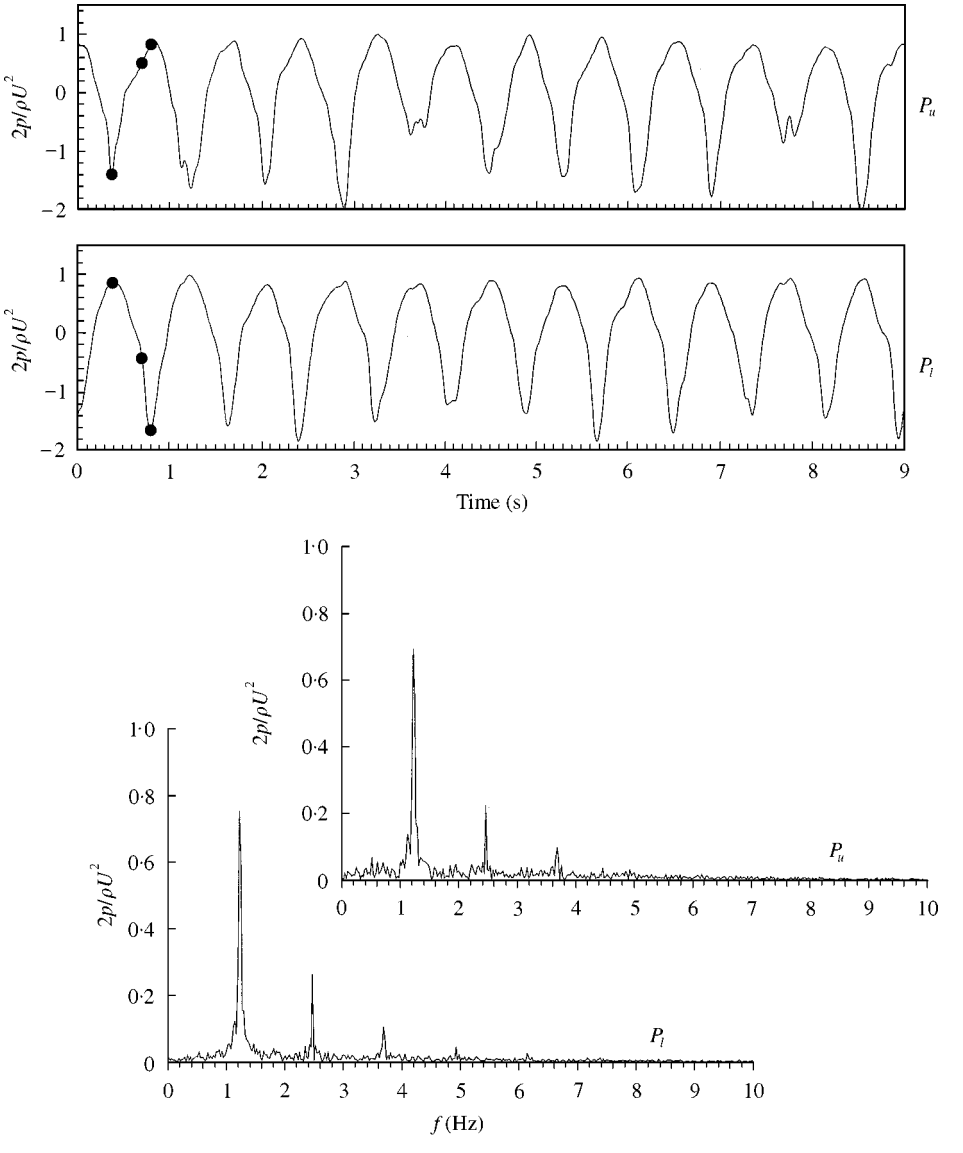

Figure 7. Pressure traces corresponding to highly resolved cinema sequence. Instants at which three representative images were acquired are represented by circular symbols. These images show the transformation from minimum to maximum pressure on the upper surface of the edge and maximum to minimum pressure on the lower surface of the edge. Sampling time is $\Delta t = 0{\cdot}005$ s.

beneath the surface of the edge. In the bottom image, which shows the instantaneous velocity field in the reference frame moving with $0{\cdot}5\bar{U}_m$, it is evident that the velocity vectors adjacent to the upper surface of the edge are directed downwards.

Finally, in Figure 8(c), the instantaneous pressures on the upper and lower surfaces are maximum-positive and -negative, respectively. The patterns of instantaneous vorticity indicate a small-scale concentration of positive (solid line) vorticity above the upper surface of the edge, and a large-scale concentration of negative vorticity beneath the tap on the lower surface. In the reference frame moving at $0{\cdot}5\bar{U}_m$ represented in the image at the

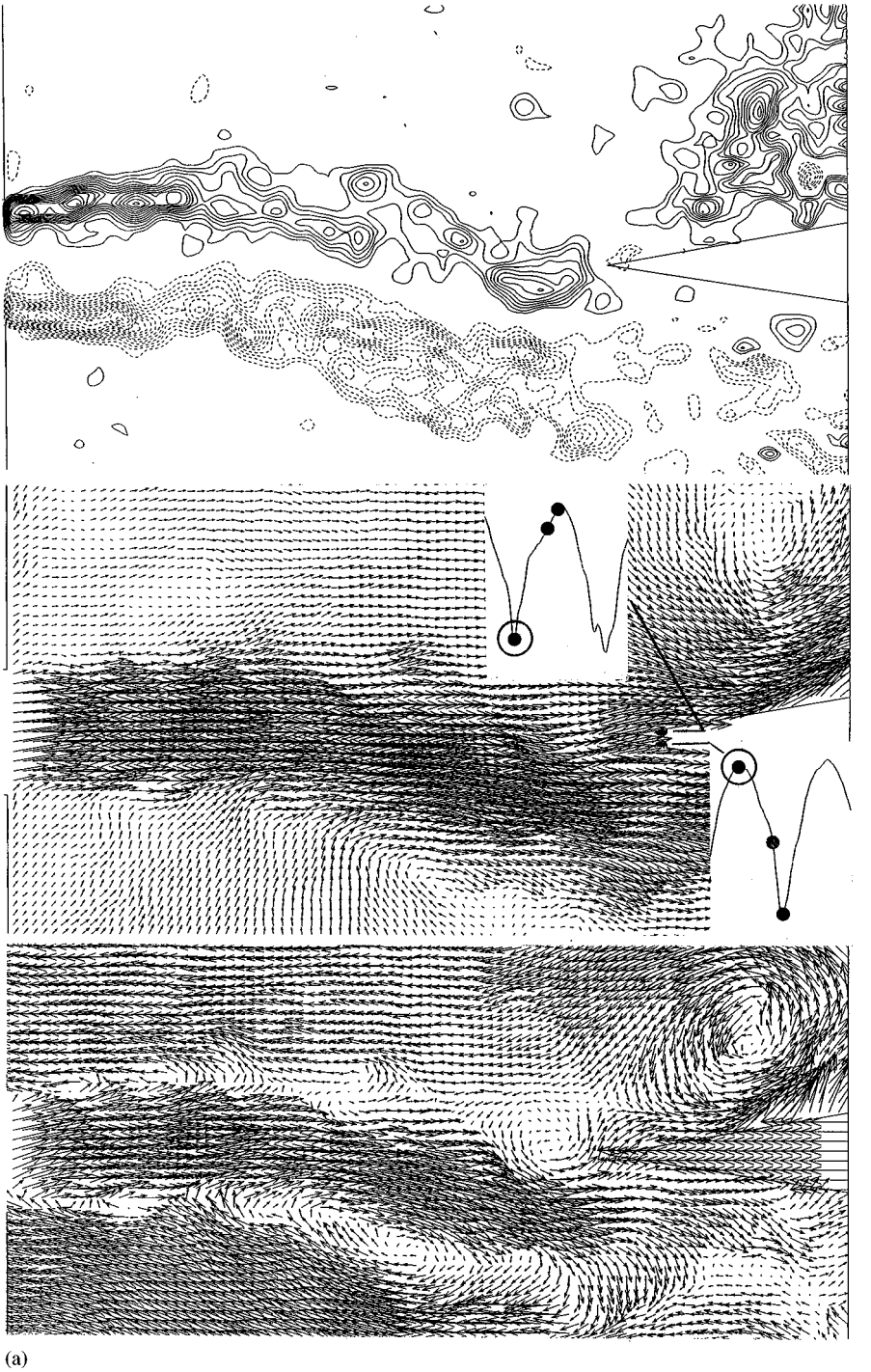

(a)

Figure 8(a). Comparison of vorticity, velocity in the laboratory frame and velocity in a frame moving at $0{\cdot}50\bar{U}_m$ for the cinema sequence. $\omega_{\min} = 10\ \mathrm{s}^{-1}$ and $\Delta\omega = 5\ \mathrm{s}^{-1}$. Images represent transformed versions of those of Lin & Rockwell (1998).

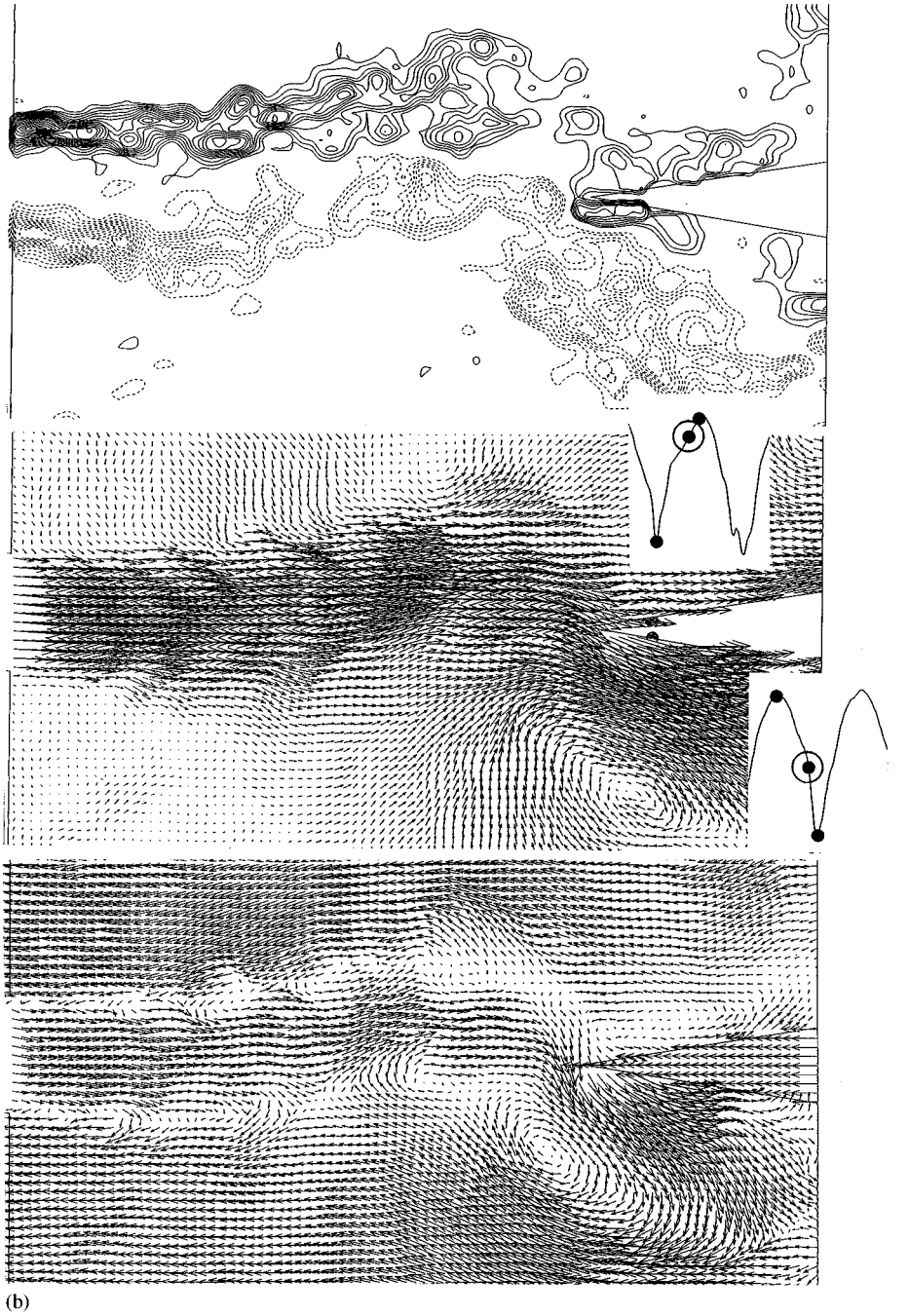

(b)

Figure 8(b). Comparison of vorticity, velocity in the laboratory frame and velocity in a frame moving at $0{\cdot}50\bar{U}_m$ for the cinema sequence. $\omega_{\min} = 10\,\mathrm{s}^{-1}$ and $\Delta\omega = 5\,\mathrm{s}^{-1}$.

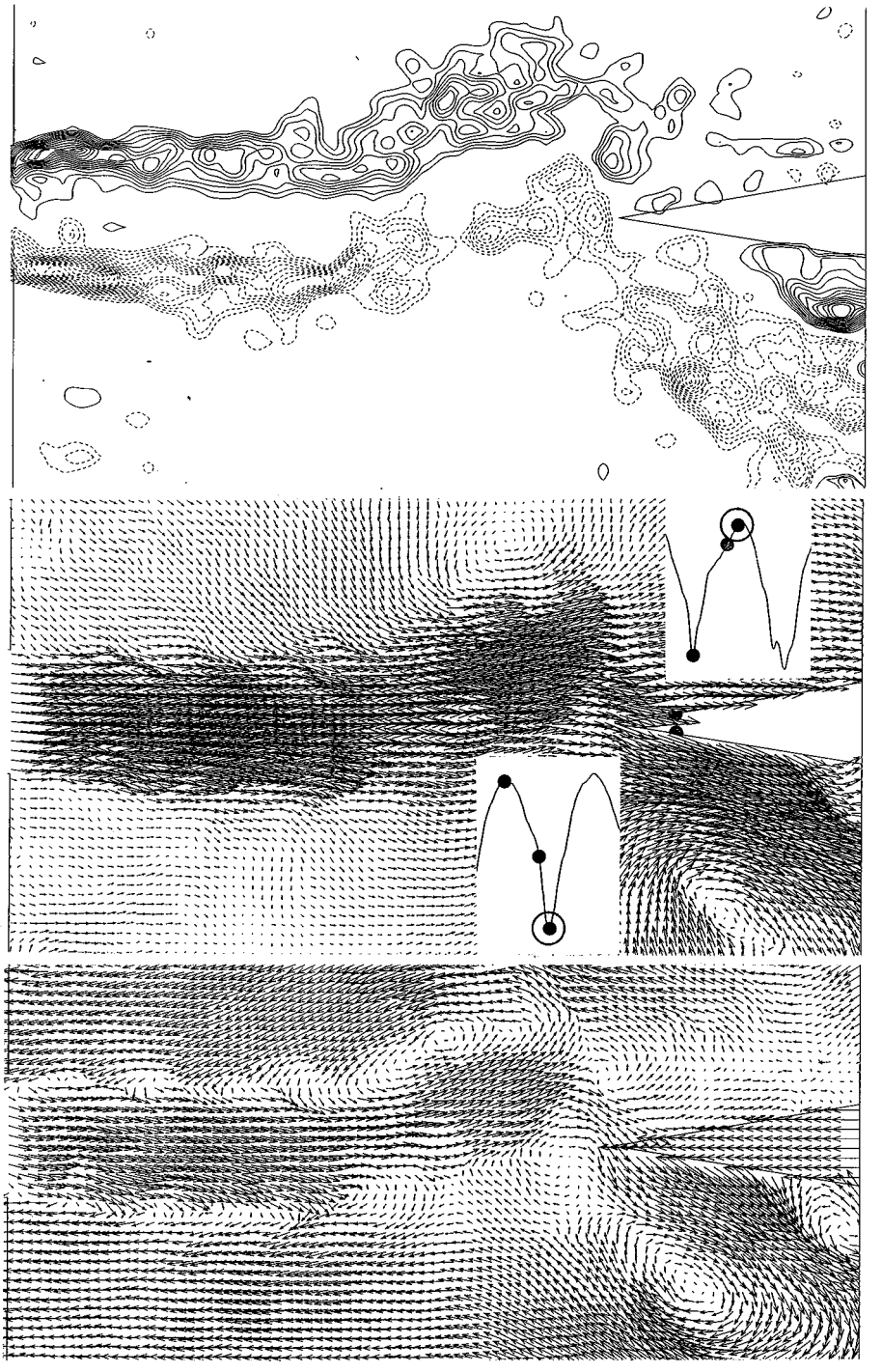

(c)

Figure 8(c). Comparison of vorticity, velocity in the laboratory frame and velocity in a frame moving at $0{\cdot}50\bar{U}_m$ for the cinema sequence. $\omega_{\min} = 10\,\mathrm{s}^{-1}$ and $\Delta\omega = 5\,\mathrm{s}^{-1}$.

bottom of Figure 8(c), the velocity vectors impinge upon the upper surface of the edge at a location approximately corresponding to the upper pressure tap.

Now that the general features of the flow physics corresponding to maximum-positive and -negative peaks of pressure have been clarified, it is appropriate to examine in greater detail the jet oscillation and its interaction with the edge. This is done by considering a segment of the pressure trace of Figure 7, in the vicinity of $t = 4{\cdot}5$ s. This segment is represented in a radically expanded form in Figure 9. These expanded segments of the upper p_u and lower p_l traces emphasize the nonlinearity of the pressure signal.

The complete sequence of images corresponding to this cinema sequence is given by Rockwell & Lin (1997). Here we show a sequence of four images, acquired at a rate of 40 frames/s, in order to illustrate the time-resolved development of the jet and its interaction with the edge.

The patterns of vorticity given in Figure 10 show increased agglomeration of vorticity into the large-scale negative (dashed line) concentration on the lower side of the jet. Simultaneously, the large-scale concentration of positive (solid line) vorticity moves downstream of the tip of the edge. Although it is possible to track certain small-scale concentrations of vorticity from one image to the next or, in some cases for several images, the exact form of these concentrations has a short half-life, no doubt due to small-scale three-dimensional effects, which are inevitable in separated flows of this type. Even though the large-scale development of the vortical structures was observed to be remarkably two-dimensional across the span of the jet, as evidenced by preliminary, qualitative dye visualization, it is unavoidable that the small-scale structures embedded within the oscillating jet experience three-dimensional distortion.

Comparing the expanded pressure trace of Figure 9 with the patterns of vorticity of Figure 10, the following features are evident over the time span represented by images 171–174. Due to the nonlinearity of the pressure signals on the upper and lower surfaces of the edge, the pressure on the upper surface decreases substantially, while that on the lower

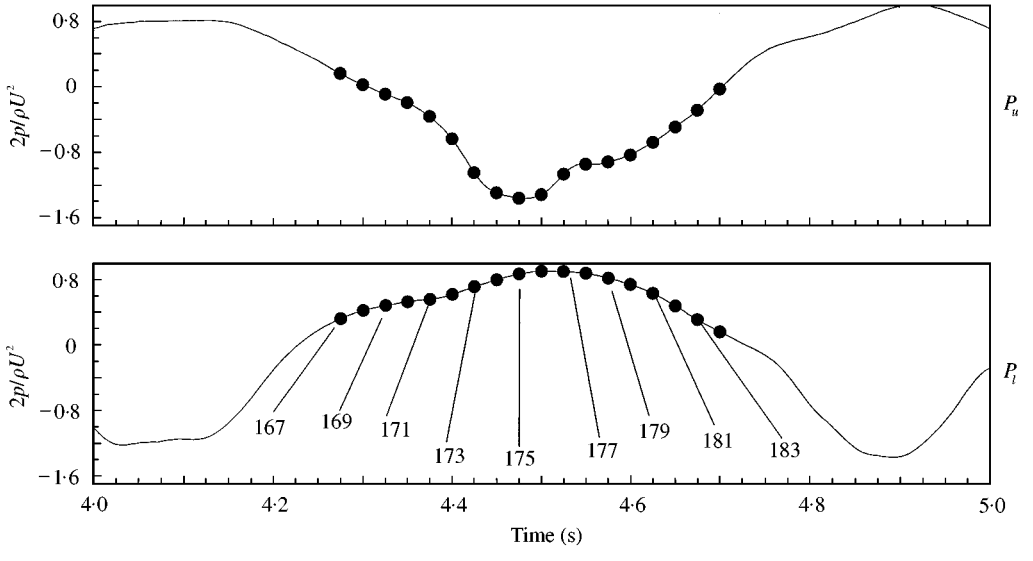

Figure 9. Expanded segment of pressure trace of Figure 7, which emphasizes the highly time-resolved image acquisition in the vicinity of maximum negative pressure p_u on the upper surface and maximum positive pressure p_l on the lower surface of the edge. Sampling time is $\Delta t = 0{\cdot}005$ s.

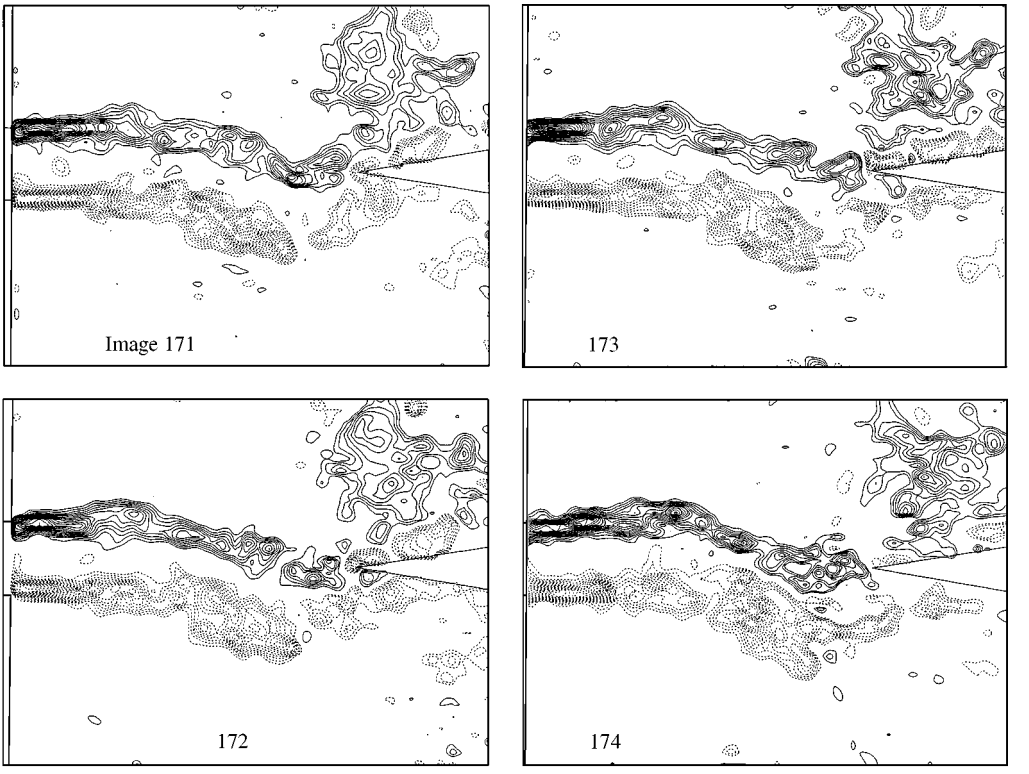

Figure 10. Excerpts from the cinema sequence showing instantaneous patterns of vorticity leading to occurrence of maximum negative pressure p_u on the upper surface and maximum positive pressure p_l on the lower surface. Images correspond to numbers 171–174, designated on the pressure data of Figure 9. Time resolution between images is $\delta t/T = 0{\cdot}03$, in which T is the period of the jet oscillation. Images represent transformed versions of those of Lin & Rockwell (1998).

surface exhibits only a mild positive increase. Correspondingly, the images of Figure 10 show that: (i) the large-scale positive (solid line) vortical structure moves downstream from the tip; and (ii) the layer of negative (dashed line) vorticity, previously severed at the tip of the edge prior to image 171, generally moves downstream along the upper and lower surfaces of the edge. The concentrations of negative vorticity between the large-scale positive vortex and the outer surface of the edge are not to be confused with what one might expect if the circulation of the large-scale vortex is sufficiently large, namely eruption of the surface boundary layer and formation of a negative region of vorticity. This scenario does not occur for the interactions illustrated in Figure 10, and the apparent secondary negative vortex is simply due to severing of the incident layer of negative vorticity in the leading region of the edge. A conceptually similar interpretation can be inferred from the images of Figures 5, 6(a) and 8(b).

5.2.2. *Coexisting instabilities in the oscillating jet*

Consideration of all of the aforementioned images reveals, first of all, development of an instability that results in a large-scale concentration of vorticity in the vicinity of the leading edge. This observation suggests that the jet oscillation arises from the inviscid amplification of an unstable disturbance in the jet. If this is indeed the case, then it should be possible to

approximate the dimensionless frequency of oscillation on the basis of the inviscid stability analyses described by Sato (1960), Betchov & Criminale (1966), and Bajaj & Garg (1977). The value of frequency predicted on the basis of inviscid analysis will be influenced by the detailed shape of the unsteady velocity distribution and whether inviscid temporal or spatial analysis is employed. On the basis of these previous studies, it is possible to infer an approximate dimensionless oscillation frequency of $\omega = 2\pi fH/U = 0{\cdot}3$. For the fundamental $k = 1$ mode shown in the plot of Figure 4, the dimensionless frequency fL/U has a representative value of $fL/U = 0{\cdot}42$, corresponding to a value of $\omega = 0{\cdot}27$. We therefore see remarkable agreement between inviscid theory applied to the organized, fundamental component of the oscillation growing on the turbulent background of the jet. The above-mentioned comparisons between pressure traces and the formation of large-scale concentrations of vorticity have revealed that the pressure signatures, formation of large-scale vorticity concentrations, and the overall undulation of the jet are highly organized and repetitive. The alternating, out-of-phase formation of the large-scale structures along the lower and upper sides of the jet is sustained by the upstream influence or feedback from the edge region, which, in turn, exerts an out-of-phase, dipole-like perturbation of the transverse velocity fluctuation at the frequency corresponding to the large-scale concentrations of vorticity. So, in essence, this means that the initial perturbations in the vicinity of the channel exit associated with development of the large-scale concentrations are essentially π-out-of-phase on the lower and upper sides of the shear layer (Powell 1961; Stabuli & Rockwell, 1987).

Coexisting with these large-scale vortical structures are small-scale concentrations of vorticity, which rapidly develop immediately downstream of the separation corners of the channel exit, evident in all of the aforementioned images exhibiting contours of constant vorticity. In fact, the agglomeration of a number of the small-scale concentrations of vorticity make up the large-scale concentrations. The identity of these smaller scales persists, in some cases, well after the large-scale concentrations become evident. In contrast to the aforementioned large-scale structures, the initial development of the small-scale concentrations of vorticity, which occurs at a much higher frequency, is not subjected to a rhythmic, out-of-phase upstream influence. In other words, the small-scales in the shear layers immediately downstream of the channel exit develop freely without local "forcing" associated with the upstream influence. The consequences are two-fold: the evolution of the small-scale concentrations is not as distinct and organized as for the large-scale concentrations; and the phase shift between the development of the small-scale concentrations on the lower and upper sides of the jet has no particular fixed value.

In order to emphasize these points, spatial distributions of instantaneous vorticity were extracted from the instantaneous cinema images 171–174 of Figure 10. The result is shown in Figure 11. The upper set of instantaneous vorticity distributions is along a horizontal line emanating from the upper corner of the channel exit and the bottom set is correspondingly along a line from the bottom corner. This space–time portrayal exhibits significant irregularity, arising primarily from the aforementioned lack of external "forcing" of the small-scale concentrations of vorticity, resulting in local three-dimensionality and an early tendency towards vortex merging. As a visual guide, inclined dashed lines, all having the same slope, indicate families of peak values of vorticity and the manner in which they change with time. The movement of the peak value of vorticity in the downstream direction provides the phase speed c_v of the small-scale concentrations of vorticity. This information can be combined with the averaged wavelength between small-scale concentrations to give a typical frequency $f = c_v/\lambda = 15{\cdot}6$ Hz. In dimensionless terms, $\omega = 2\pi fH/\bar{U}_m = 2{\cdot}82$.

It is therefore evident that this predominant frequency of formation of the small-scale concentrations of vorticity lies well above the aforementioned frequency of the large-scale

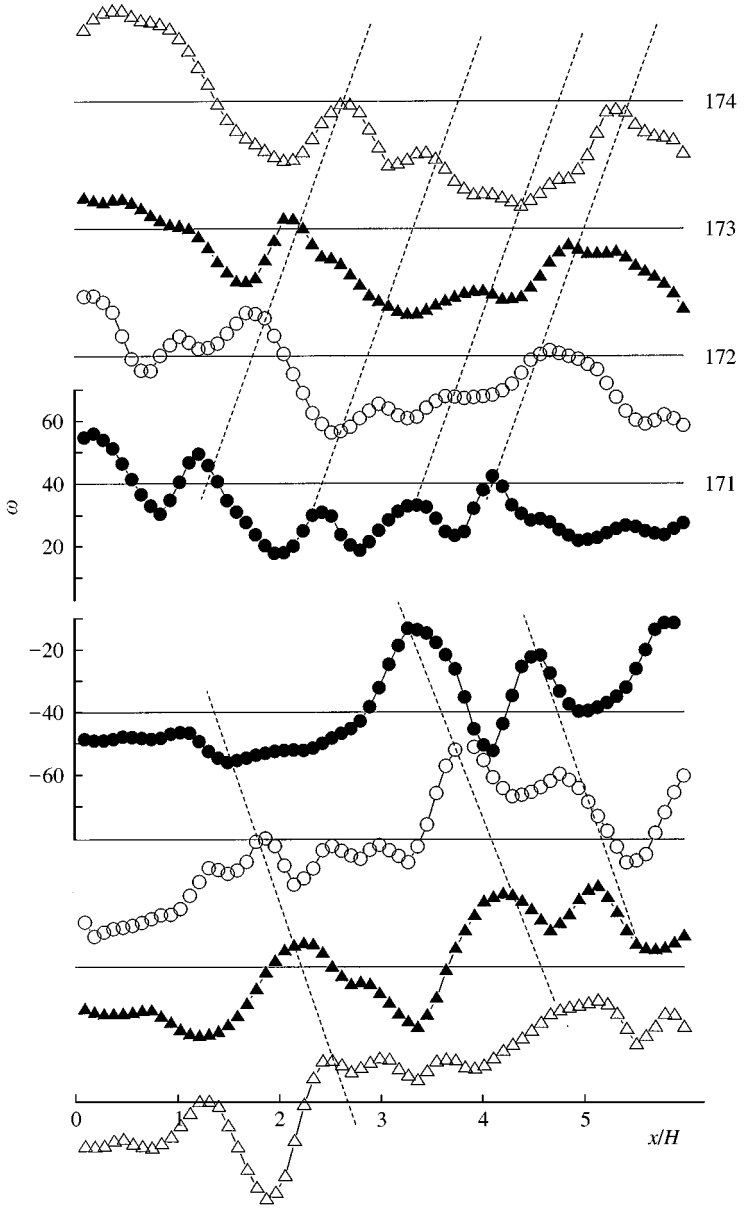

Figure 11. Spatial distributions of vorticity along horizontal lines extending from the corners of the channel exit for sequential instants of time corresponding to images 171–174. Inclined dashed lines are intended to serve as a guide for identifying common peaks or valleys, corresponding to maxima and minima of vorticity concentrations. These data were extracted from the images of Figure 10.

concentrations, which scales on the overall jet half-width H. It is clear from the images of instantaneous vorticity that the small-scale concentrations are confined to a narrow band of the shear layer in the immediate vicinity of the corner of the channel exit. In turn, the slope of the time-averaged velocity profile $\mathrm{d}\bar{u}/\mathrm{d}y$ in this region is very large, due to the existence of the fully developed turbulent channel flow. As a consequence, the local vorticity thickness $\delta_\omega = \Delta\bar{U}/(\mathrm{d}\bar{u}/\mathrm{d}y)_{\max}$, in which $\Delta\bar{U}$ is the velocity difference across the shear layer, will be

small relative to that occurring in a fully evolved jet shear layer well downstream of the nozzle exit, where the large-scale vortical structures develop. Further efforts should evaluate δ_ω and interpret dimensionless frequencies in accord with the theory of Huerre & Monkewitz (1990). This origin of the small-scale vortical structures should then be assessed in conjunction with pre-existing, small-scale structures in the turbulent shear flow upstream of separation.

5.2.3. *Interpretation of large-scale vortex interaction with leading edge*

An early model for the onset and development of the jet oscillation in a jet–edge system was advanced by Powell (1961), who recognized the importance of unstable disturbance amplification in the jet and by Holger *et al.* (1977), who accounted for the growth and interaction of the large-scale vortex street with the edge, in order to predict the frequency and hydrodynamic feedback originating at the edge. A schematic of the model of Holger *et al.* (1977) is given in the inset (bottom) of Figure 12. In essence, they take the vortex street to be fully formed by the time it reaches the edge. It is evident, however, from the vorticity distributions of the foregoing images of Figures 5, 6, and 8 that the large-scale vortices have highly distributed vorticity and a noncircular form. The evolution of a cluster of vorticity corresponding to formation of a single large-scale vortex as a function of time is illustrated in Figure 12. It is evident that the terminal state, represented by the vortex from image 184,

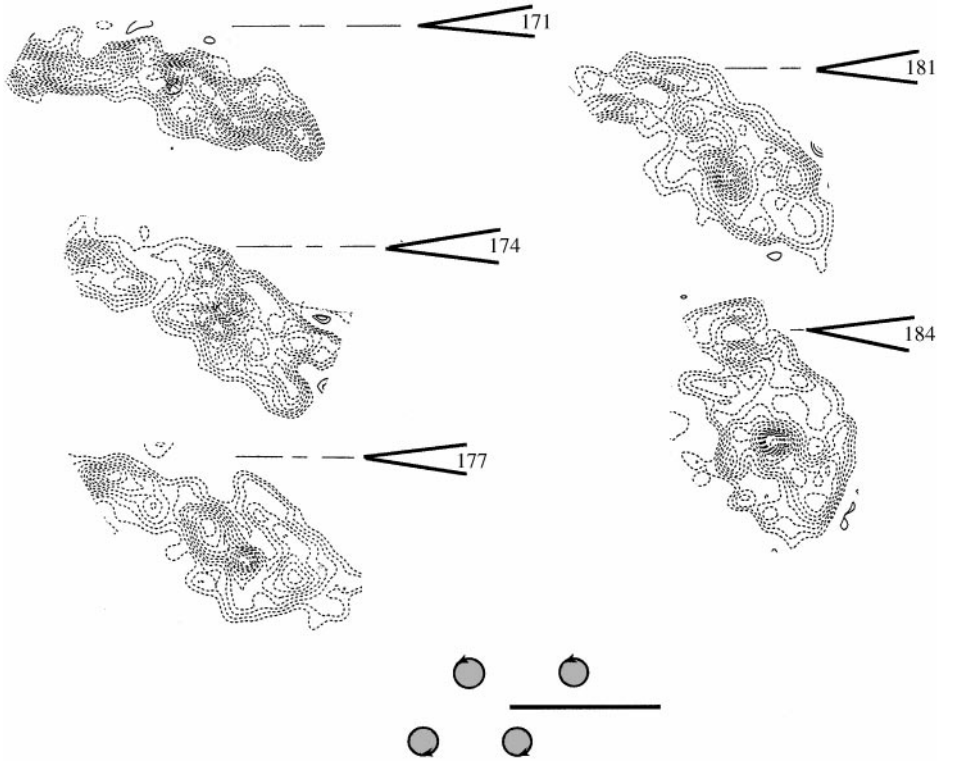

Figure 12. Evolution of a defined cluster of vorticity, which eventually evolves into a large-scale vortex as it encounters the impingement edge. Images were extracted from the same cinema sequence as Figure 10. Horizontal reference lines correspond to the plane of symmetry of the jet–edge system, i.e., the line passing through the tip of the edge. The dimensionless circulation Γ^* is constant for all clusters of vorticity.

is a well-defined vortex with a dimensionless circulation $\Gamma^* = \Gamma/\pi\bar{U}_m 2H = 1{\cdot}11$. Using this value of Γ^* as a reference, and working backwards in time through images 181, 177, and 171, the location of the cut-off of the upstream boundary of the large-scale vortex was adjusted to give the same value of Γ^* as for the terminal vortex in image 184. This procedure allows reconstruction of the time evolution of a defined cluster of vorticity having a constant value of circulation. In image 171, the vorticity is relatively concentrated in a thin, highly elongated layer and, with increasing time, evolves towards a larger-scale cluster of vorticity in images 174 and 177. Simultaneously, the cluster of vorticity rotates in the clockwise direction, particularly evident in image 181 and, finally, in image 184, the major axis of the elliptically shaped pattern of vorticity is nearly vertical. On the basis of these observations, it is evident that the large-scale vortex continues to evolve in form and orientation, even as it encounters the tip region of the edge; moreover, the location of the centroid of the vorticity concentration measured from the plane of symmetry of the edge, increases with time.

An important observation concerns the possible shedding of a secondary vortex in the tip region of the edge. Examination of, for example, the vorticity distribution in the vicinity of the tip of the edge in Figure 10 shows a region of positive vorticity immediately below the surface of the edge and above the large-scale negative concentration of vorticity. This positive vorticity is simply that on the opposite (upper) side of the jet; it has not agglomerated into a large-scale vortex, but has been severed at the tip of the edge. In other words, the large-scale negative vortex of Figure 10 has not induced shedding of a vortex either from the tip of the edge, which was considered to be a key component of the jet edge interaction by Curle (1953), or from the continuous surface of the edge, as may occur for different configurations of vortex–edge interaction, as shown by Jefferies & Rockwell (1996). In fact, positive vorticity can exist simultaneously on both the lower and upper sides of the edge due to severing of the upper vorticity layer at the tip.

5.2.4. *Relation of vortex–edge interaction to potential generation of acoustic power*

The instantaneous hydrodynamic field represented by the vorticity distributions of Figure 10, as well as by the corresponding velocity distributions (Lin & Rockwell 1998), plays a central role in determining the acoustic power generation, in the event that a resonant acoustic field exists simultaneously with the hydrodynamic field. According to the formulation of Howe (1975, 1980, 1984), the instantaneous acoustic power generation P is given by

$$P = -\rho \int_{\forall} < (\boldsymbol{\omega} \times \mathbf{V}) \cdot \mathbf{u} > \mathrm{d}\forall, \tag{1}$$

in which $\mathbf{u}$ is the vector acoustic velocity at a given point, $\mathbf{V}$ is the vector hydrodynamic velocity and $\boldsymbol{\omega} \times \mathbf{V}$ is the curl of the vorticity with the hydrodynamic velocity. It should be noted that this relation is relevant to any sufficiently long wavelength sound wave, not just resonant ones. Hourigan *et al.* (1990) have physically interpreted equation (1) for the occurrence of resonance in the configuration of a baffle-cavity using smoke visualization in conjunction with a discrete vortex simulation.

The aim of our present considerations is to interpret the hydrodynamic contribution $\boldsymbol{\omega} \times \mathbf{V}$ using instantaneous spatial representations of $\boldsymbol{\omega}$ and $\mathbf{V}$. It should be kept in mind that if the jet exists in a mode of resonant coupling with a resonator, its structure will be modified relative to that shown herein. The intent of the present evaluation is to demonstrate the nature of $\boldsymbol{\omega} \times \mathbf{V}$ for a representative turbulent jet. The distribution of vectors $\boldsymbol{\omega} \times \mathbf{V}$ for the present jet–edge interaction is shown in the region of the edge for images 171 and 173 in

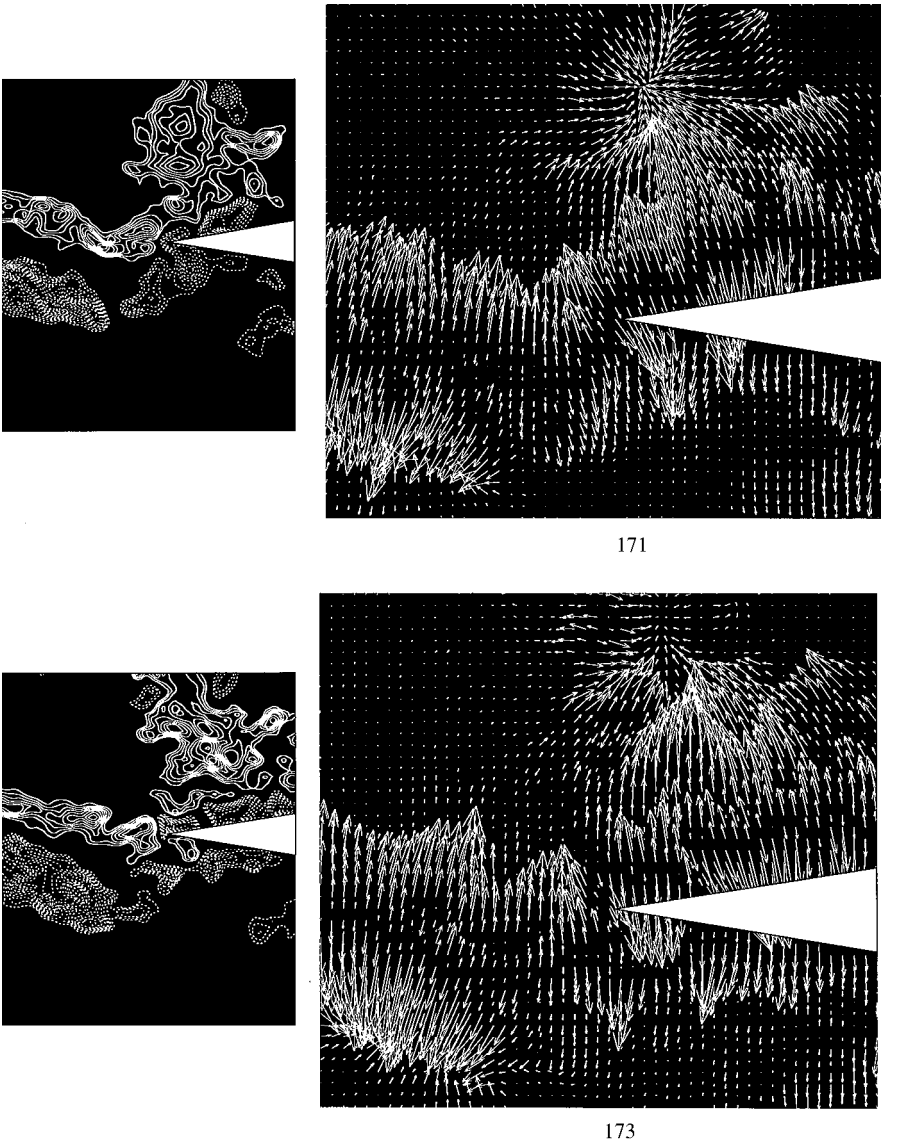

Figure 13. Contours of constant vorticity for images 171 (top) and 173 (bottom) of the cinema sequence of Figure 10 and corresponding vectors of the quantity $\boldsymbol{\omega}\times\mathbf{V}$ of the acoustic power integral.

doi:10.1006/jfls.2000.0380

Figure 13. In image 171, the large-scale vortical structure above the edge generates a sink-like pattern of vectors, whereas all other vorticity concentrations produce predominantly vectors oriented in the positive or negative vertical direction. Particularly notable are the substantial contributions from the small-scale vortical structures, including those along the upper surface of the impingement edge. In image 173, the clusters of vectors along the edge surface are particularly pronounced and, furthermore, the large-scale structure above the edge loses its sink-like character. The importance of the small-scale concentrations of vorticity in generating substantial magnitudes of $\boldsymbol{\omega}\times\mathbf{V}$ is evident in both images 171 and 173. Moreover, these images, which exhibit vectors oriented predominantly in the vertical direction, suggest that resonant acoustic waves having velocities $\mathbf{u}$ oriented in the vertical direction will provide particularly large contributions to the acoustic power P, since the value of the dot product in equation (1) will be maximum. The converse holds for a resonant wave oriented in the horizontal direction.

5.2.5. *Phase-referenced representations of vortex–edge interactions*

As noted in the foregoing, a cinema sequence having lower temporal resolution, but extending over approximately nine complete cycles of oscillation, was acquired in order to determine the degree to which the jet structure was phase-locked from cycle to cycle. Complete details, along with sets of images, are given by Rockwell & Lin (1997). Figure 14 shows a sequence of images, each acquired at the same phase of the instantaneous pressure signal on the lower surface of the impingement edge. This phase-referenced condition

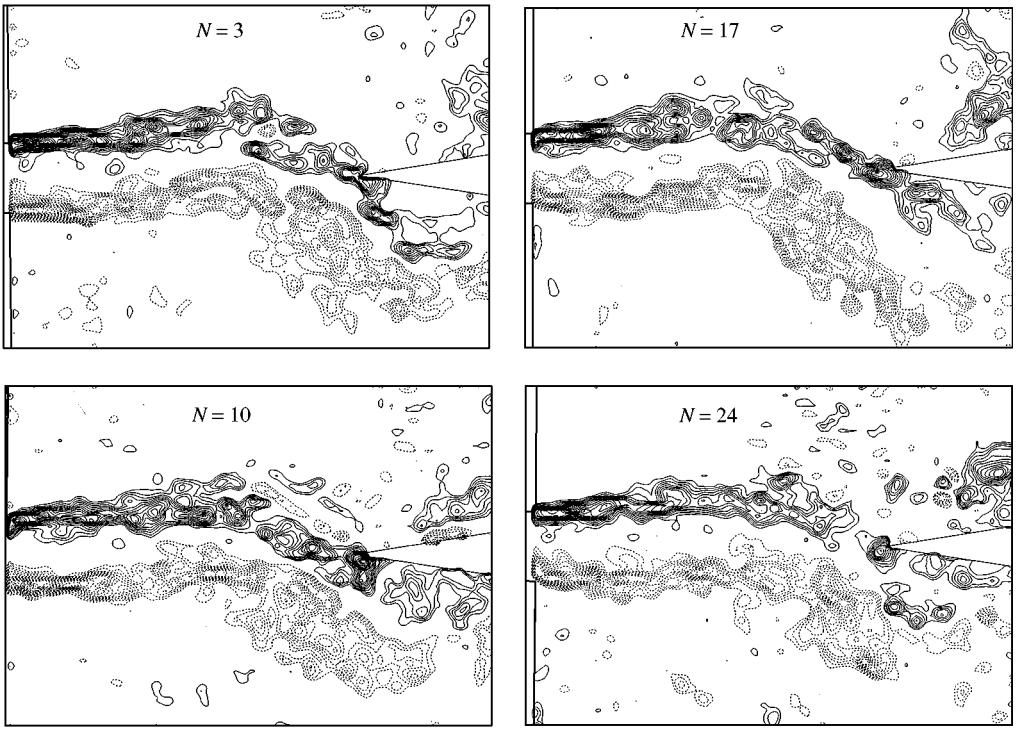

Figure 14. Representative images of the phase-referenced vorticity field excerpted from cinema sequence; each image corresponds approximately to occurrence of zero instantaneous pressure p_l on the lower surface of the impingement edge.

corresponds to frame numbers $N = 3$, 10, 17 and 24. In all images, a large-scale concentration of negative (dashed line) exists on the lower side of the jet at a location just upstream of the impingement edge. Moreover, the positive layer of vorticity, originating at the channel exit and exhibiting a train of small-scale vorticity concentrations, intersects the tip of the edge. Remarkable is the fact that an extremum of the small-scale concentrations of positive vorticity centered at the tip of the edge is well defined in all images. Finally, a portion of the large-scale concentration of vorticity on the upper surface of the edge is evident in all images. It is evident that the large-scale vorticity concentrations are generally phase-repetitive, i.e., tend to occur at approximately the same location with a generally similar form of each of the images. With the exception of the small-scale concentration at the tip of the edge, there is no such phase consistency or phase-locking of the small-scale concentrations of vorticity.

6. ENSEMBLE-AVERAGED STATISTICS OF JET–EDGE INTERACTION

In order to determine the averaged statistics of the jet–edge interaction, both the randomly acquired and cinema sequences of images were employed. The procedure was the same for both sequences. In essence, successive images were "stacked" such that at a given coordinate (x, y), the instantaneous values of velocity u, v were determined at that coordinate location. Then, using the equations defined in the following, the various statistical representations were calculated. For the randomly acquired sequence, this involved a total of 36 images at a minimum time interval of 10 s. The time scale of the jet oscillation is of the order of 1 s, so the minimum sampling interval is approximately a factor of 10 larger. This random sampling is typical of that employed in turbulent flows. An example is the averaged turbulent statistics of a turbulent jet impinging upon a plate involving 11 images (Landreth & Adrian 1990). For the cinema sequence with low time resolution, it involved a total of 35 images, acquired at a nominal spacing of 114 ms, over a total number of five cycles, i.e., $5T$, in which T is the period of the jet oscillation. The equations employed for determining the ensemble-averaged statistics are defined as follows:

$$\langle V \rangle \equiv \frac{1}{N} \sum_{n=1}^{N} V_n(x, y), \tag{2}$$

where $\langle V \rangle \equiv$ averaged (or mean) total velocity. Similar definitions hold for the horizontal u and vertical v velocity components and for the vorticity ω. For the fluctuating components, u_{rms}, the root-mean-square of u component fluctuation, is given by

$$u_{\text{rms}} \equiv \langle u \rangle_{\text{rms}} \equiv \left[\frac{1}{N} \sum_{n=1}^{N} [u_n(x, y) - \langle u(x, y) \rangle]^2 \right]^{1/2} \tag{3}$$

and similarly for the root-mean-square of the v component fluctuation, v_{rms}. For the Reynolds stress, the averaged value of Reynolds stress correlation, $\langle u'v' \rangle$, is

$$\langle u'v' \rangle \equiv \frac{1}{N} \sum_{n=1}^{N} [u_n(x, y) - \langle u(x, y) \rangle] [v_n(x, y) - \langle v(x, y) \rangle]. \tag{4}$$

We emphasize that, unlike some ensemble-averaging processes, no phase reference or phase trigger was employed. Rather, in the case of the randomly acquired images, the camera was triggered at an arbitrary time, as long as the interval between images was greater than 10 s. Likewise, for the cinema series, no phase condition was employed. For the cinema sequence, the spacing between successive images employed in the ensemble-averaging process is of the order of 1/10th the predominant period of the jet oscillation.

Since markedly different criteria were employed for the acquisition of images, i.e., random versus continuous cinema, a direct comparison of the averaged quantities should provide an indication of the degree of convergence. For this reason, averaged images obtained from the cinema sequence are directly compared with those from the randomly acquired series in the figures that follow. Each figure contains two averaged images. The top one corresponds to that obtained from the cinema sequence, while the lower one represents the randomly sampled (acquired) sequence.

The ensemble-average of the total velocity V in the laboratory frame is shown in Figure 15. In this image, as well as in all subsequent ensemble-averaged representations, the region in the immediate vicinity of the edge has been blanked out, due to uncertainties associated with image registration. The patterns of vectors exhibited in Figure 15 are generally antisymmetrical with respect to the plane of symmetry of the edge. The ensemble-averaged vorticity of Figure 16 exhibits very high levels of $\langle\omega\rangle$ in the immediate vicinity of the corners of the channel exit. This averaged vorticity overshadows the remarkably low levels of vorticity in the vicinity of the impingement edge.

Contours of constant u_{rms} are shown in normalized form in Figure 17. Relatively high levels are attained in the shear layers of the jet, especially at a location approximately three nozzle widths downstream of the channel exit. In addition, high levels occur on the upper and lower sides of the edge, at a location immediately downstream of the tip.

Corresponding contours of v_{rms}, normalized with respect to the maximum velocity, are given in Figure 18. They also exhibit relatively high values in the vicinity of the tip of the edge. In this case, a particularly large magnitude is centered at the tip. In comparison, the foregoing extrema of the u_{rms} contours are located immediately downstream of the tip adjacent to the upper and lower surfaces.

The ensemble-averaged Reynolds stress patterns of Figure 19 exhibit large values of $\langle u'v'\rangle$ in the shear layers of the jet at a distance approximately three to four nozzle widths downstream of the nozzle exit. These high values of $\langle u'v'\rangle$ are clearly due to the large amplitude, transverse undulation of the jet. In addition, extrema of Reynolds stress are evident on the upper and lower sides of the tip region of the edge, again due to the severe flow distortion in that region, arising from the jet–edge interaction. In the region immediately downstream of the nozzle exit, local extrema of Reynolds stress occur due to the onset of small-scale vortices.

It is of interest to compare these extreme values of Reynolds stress with those occurring within the turbulent channel flow. Referring to Figure 2, the nominal value of peak Reynolds stress is approximately at $0{\cdot}8u_*^2$, which corresponds to $0{\cdot}0013\bar{U}_m^2$. The extreme values of ensemble-averaged Reynolds stress in the three primary regions of Figure 13 are: $0{\cdot}006\bar{U}_m^2$ in the region immediately downstream of the nozzle exit, induced by the small-scale vortex formation; $0{\cdot}020\bar{U}_m^2$ in the jet shear layers at a location three to four nozzle widths downstream of the channel exit; and $0{\cdot}047\bar{U}_m^2$ in the immediate vicinity of the tip of the edge. It is therefore evident that the averaged peak Reynolds stresses in each of these three regions exceed by factors of approximately 5, 15, and 40 the maximum Reynolds stress in the channel flow. This observation underscores the powerful influence of instabilities leading to both small- and large-scale vortex formation, which in turn are associated with the large-scale undulations of the jet.

7. CONCLUDING REMARKS

Self-sustained oscillation of a planar jet impinging upon an edge has long been recognized as a generic type of flow–structure interaction. Previous related investigations have focused on relatively low values of Reynolds number for which the jet is initially laminar at the

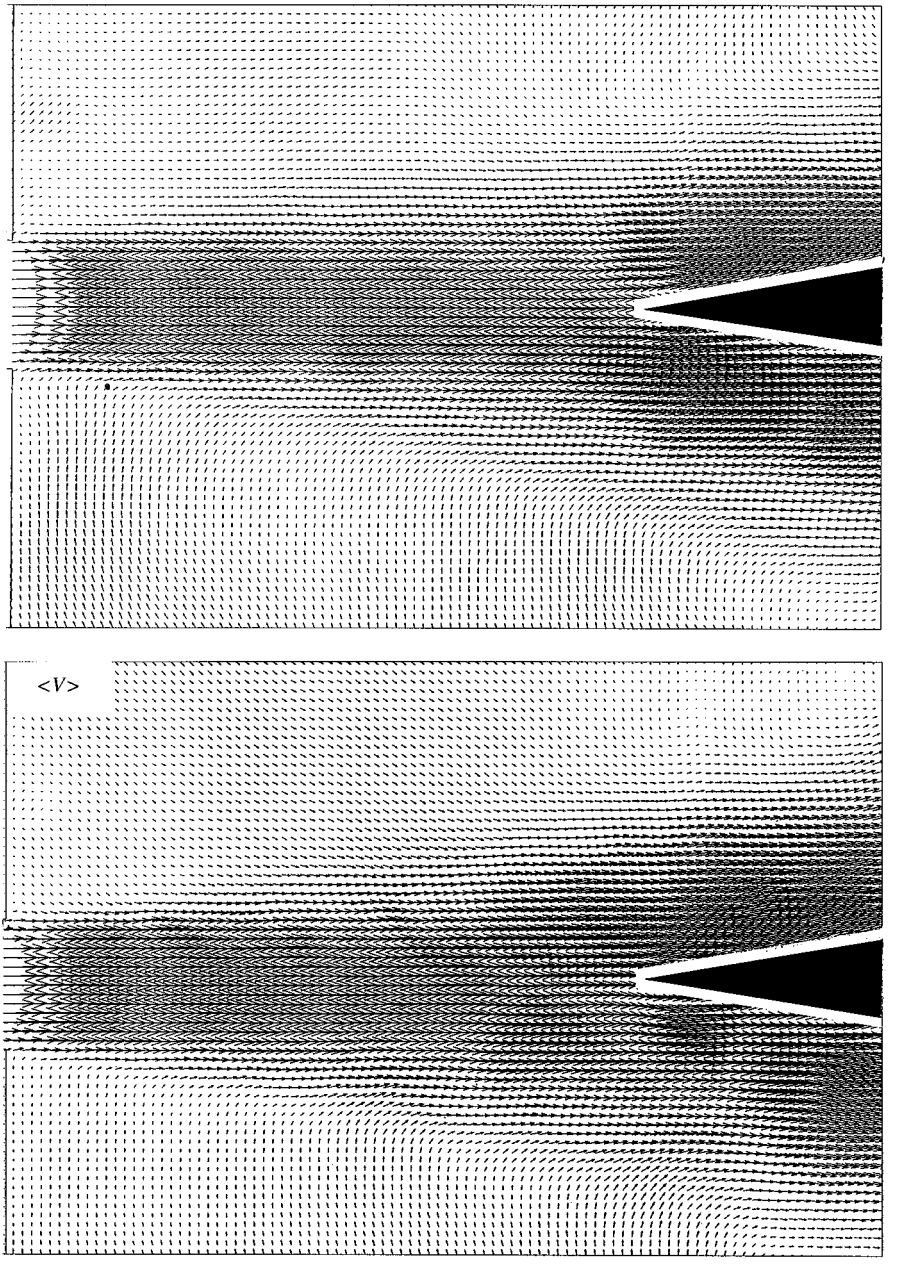

Figure 15. Ensemble-averaged distribution of total velocity $\langle V \rangle$ shown in laboratory reference frame. The top image is from cinema sequence and the bottom image is from randomly acquired sequence.

nozzle exit. Even in this limiting case of the undulating laminar jet, quantitative aspects of the flow physics, especially the interaction region near the tip of the edge, which dictates the edge loading and thereby the upstream influence, have remained unclarified. The present investigation addresses the more complex case of a jet formed from a fully turbulent channel flow. The issues of whether self-sustained oscillations can occur and the related unsteadiness

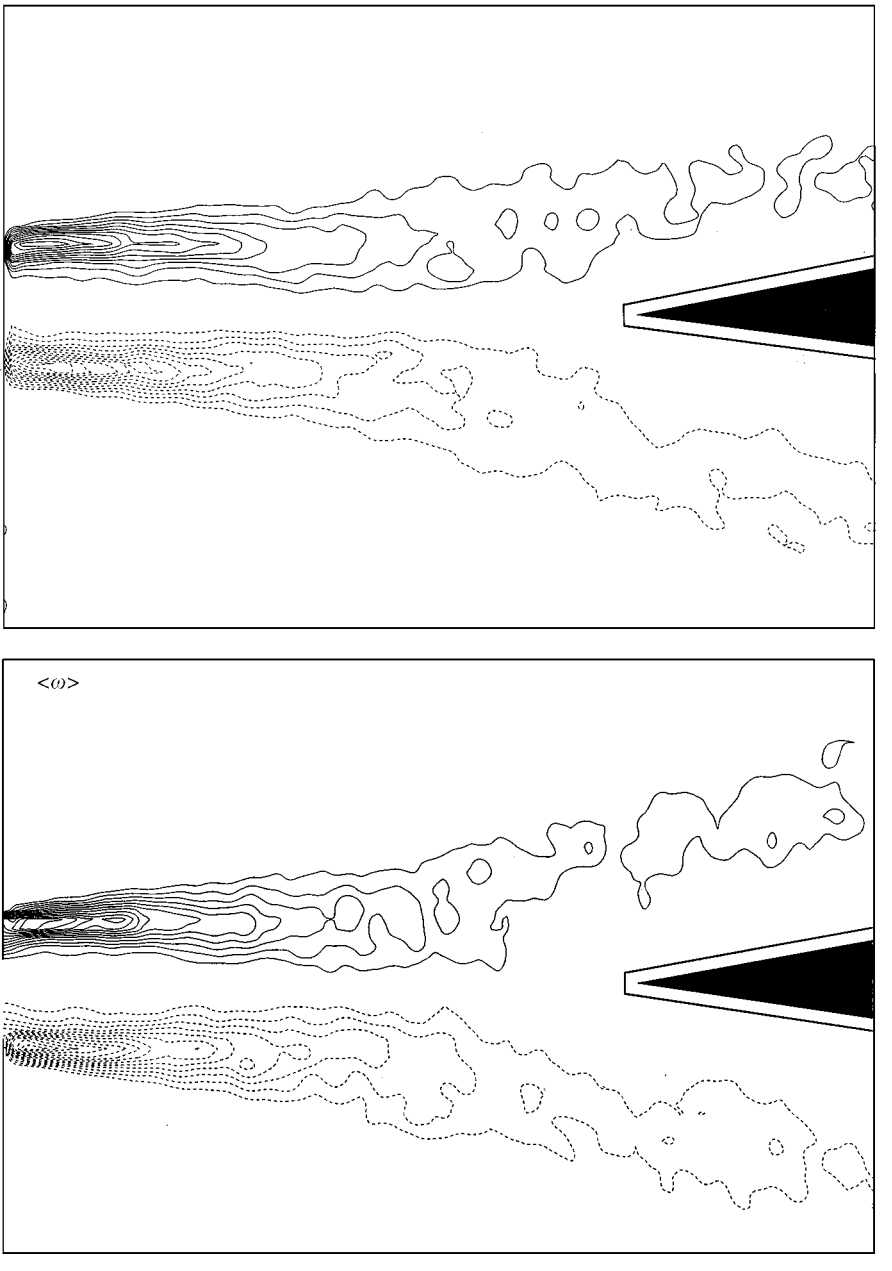

Figure 16. Contours of ensemble-averaged vorticity, $\langle\omega\rangle$. The top image is from cinema sequence and the bottom image is from randomly acquired sequence. Minimum vorticity $\omega_{\min} = \pm 10\,\mathrm{s}^{-1}$ and incremental vorticity $\Delta\omega = 5\,\mathrm{s}^{-1}$.

of the jet have been pursued. In doing so, the instantaneous structure of the initially turbulent jet, the instantaneous loading on the edge, and the averaged turbulence statistics of the jet–edge system have been characterized using a global imaging approach. It should be emphasized that, in the present experiment, the unsteadiness of the jet–edge system is strictly hydrodynamic. That is, it occurs in the absence of acoustic, or analogous free-surface, resonant modes of the flow system; moreover, fluid–elastic effects are not present.

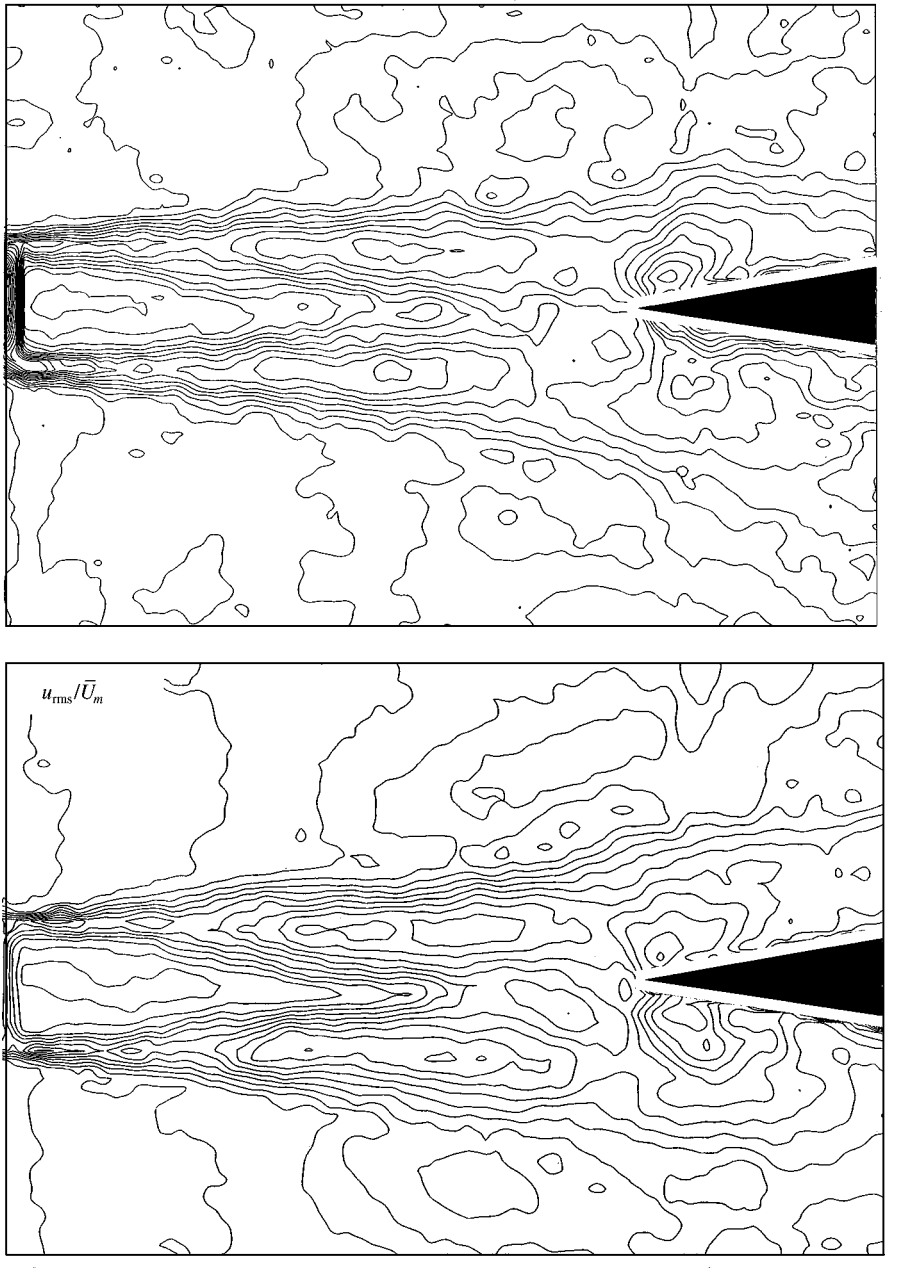

Figure 17. Contours of constant root-mean-square of the streamwise component of the velocity fluctuation, u_{rms}, normalized with respect to the maximum velocity at the centerline $\bar{U}_m$. Minimum contour is 0·02 and increments are 0·02. The top image is from cinema sequence and the bottom image is from randomly acquired sequence.

Both of these phenomena are considered parasitic for our present purposes in that they can greatly enhance coherent oscillations through coupling effects.

The principal findings are summarized in the following.

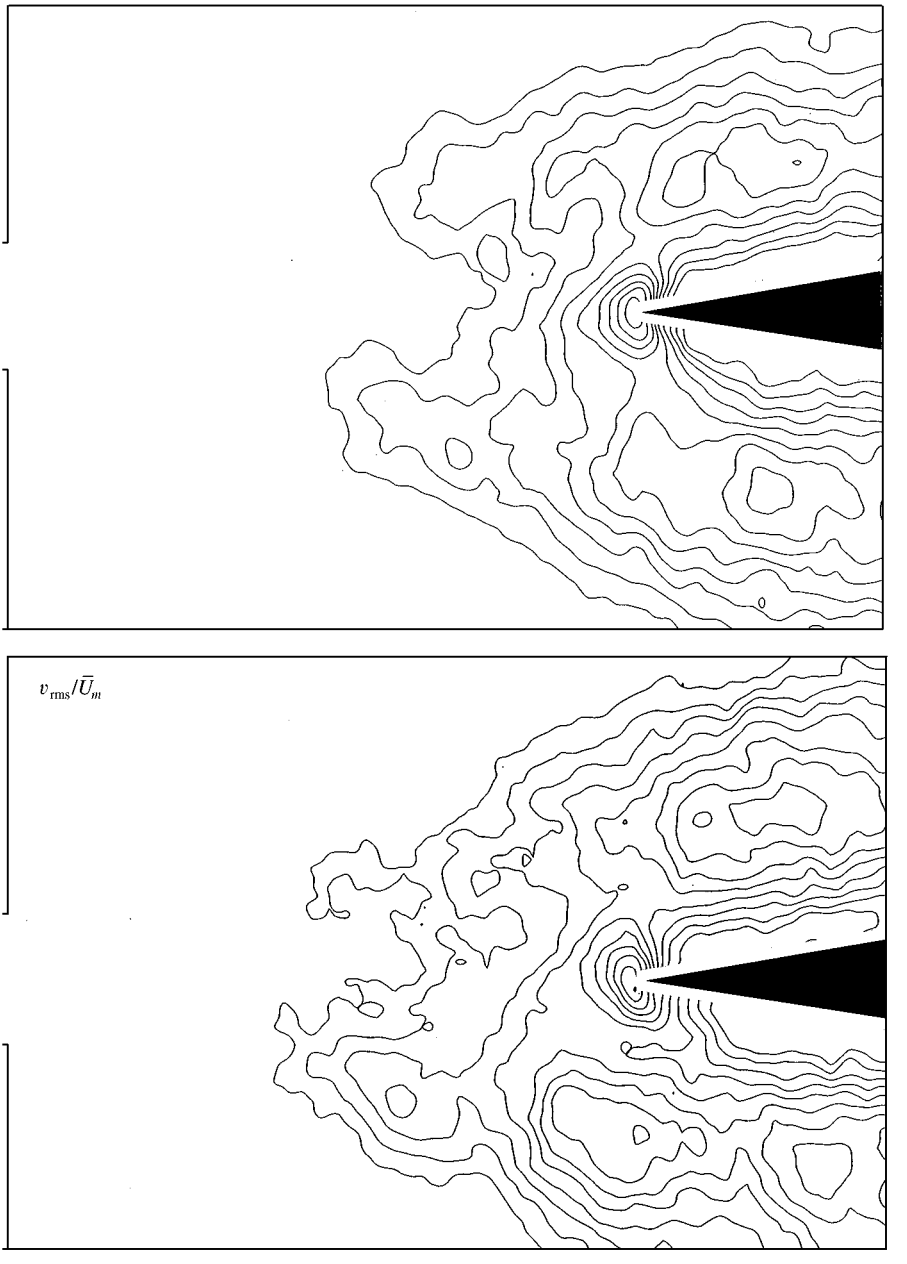

Figure 18. Contours of constant root-mean-square of the transverse component of the velocity fluctuation, v_{rms}, normalized with respect to the maximum velocity $\bar{U}_m$ at the centerline. Minimum contour is 0·02 and incremental values are 0·02. The top image is from cinema sequence and the bottom image is from randomly acquired sequence.

7.1. Instantaneous Structure of the Initially-Turbulent Jet

It has been demonstrated that the jet formed from a fully turbulent channel flow exhibits highly organized, self-sustained oscillations. The major features of the jet evolution have been characterized using images of vorticity and velocity, acquired with adequate temporal

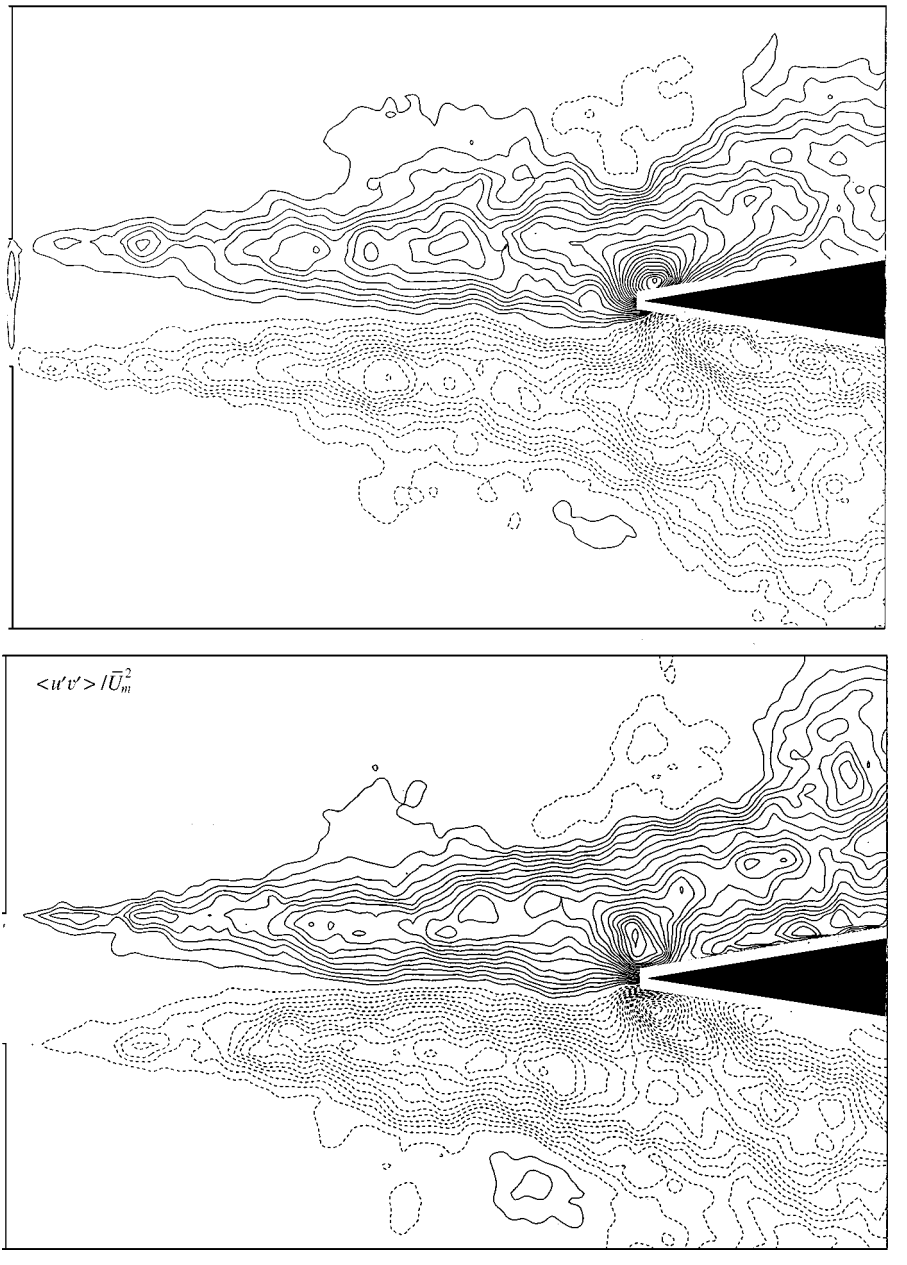

Figure 19. Contours of constant ensemble-averaged Reynolds stress, $\langle u'v' \rangle$, normalized by square of maximum velocity $\bar{U}_m^2$. The top image is from cinema sequence and the bottom image is from randomly acquired sequence. The minimum contour is 0·002 and the increment between contours is 0·002.

resolution, in order to determine the time history of the unsteadiness. In essence, these features may be stated as follows.

(a) The jet supports two clearly identifiable modes of instability of drastically different scales. The large-scale, global mode involves formation of vortices that scale on the overall

thickness of the jet. The frequency of these vortices is well approximated by application of inviscid stability theory to the averaged turbulent background flow. The small-scale, local mode gives rise to a train of small vortices having a frequency and wavelength much larger and smaller, respectively, than those of the large-scale vortices. It may scale on the local vorticity thickness of the inner region of the boundary layer at the separation edge; further theoretical assessment is required. Interpretation in conjunction with small-scale structures in the approach turbulent boundary layer is needed.

(b) The two-scale instability of the impinging turbulent jet is, in some respects, analogous to the two-scale instability in the near-wake of a circular cylinder at sufficiently high Reynolds number, as represented by the comparison of Figure 20. In the case of the wake,

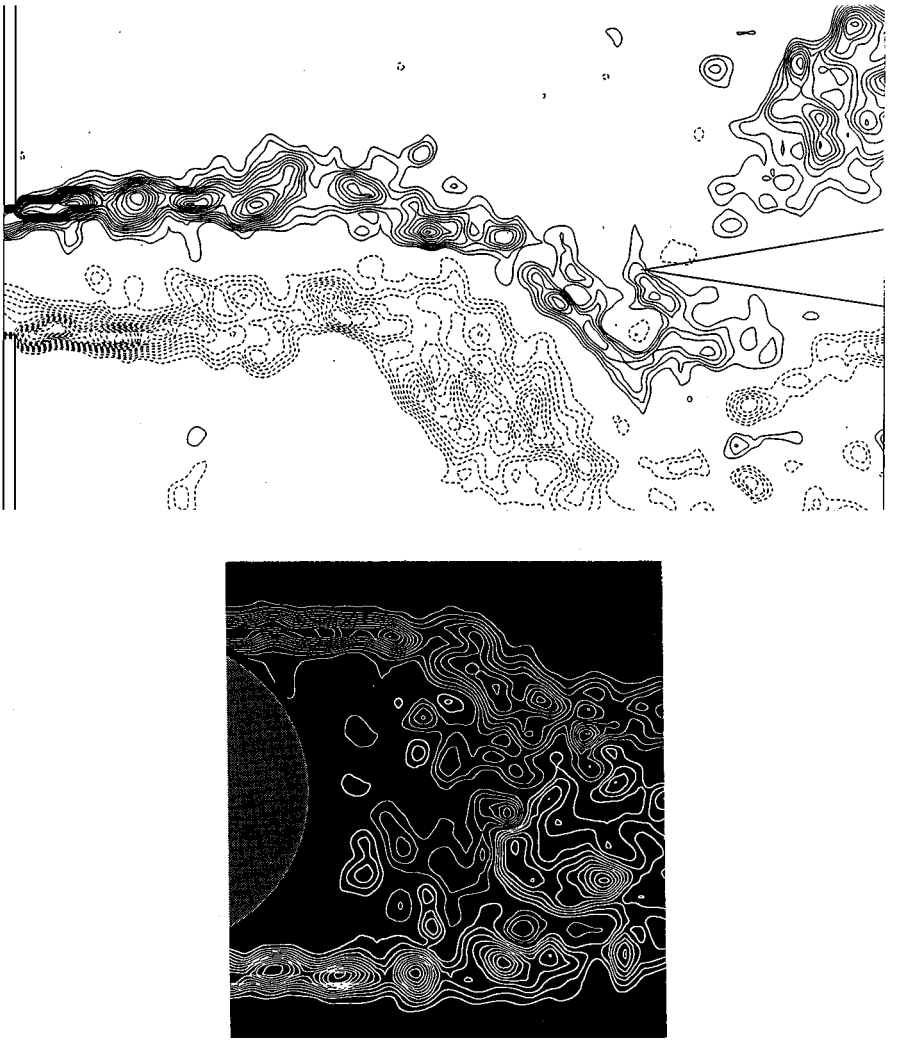

Figure 20. Comparison of the near-wake of a circular cylinder and the jet in a jet–edge system. Both exhibit the rapid development of small-scale vorticity concentrations due to a localized instability immediately downstream of separation of the shear layer. The Reynolds number for the flow past the cylinder, based on cylinder diameter, is 10 000 [from Chyu & Rockwell (1996)]. Note that the bottom shear layer from the circular cylinder exhibits a train of small-scale vortices that roll up to form the Kármán vortex. For the jet-flow, the Reynolds number, based on nozzle width, is 10 944.

small-scale vortices formed in the thin shear layer immediately downstream of separation coalesce to form the large-scale Kármán vortices. For both the impinging turbulent jet and the turbulent near-wake of the cylinder, the large-scale vortices emerge as highly coherent vortical structures. For the near-wake, it is well known that the existence of a global (absolute) instability promotes the onset of highly robust, limit-cycle oscillations, which correspond to generation of the large-scale vortices (Huerre & Monkewitz 1990). The upstream influence required to attain these large-scale oscillations is inherent to the concept of the global or absolute instability, which accommodates an upstream wave.

On the other hand, for the impinging turbulent jet, the jet instability is convective, as opposed to absolute, but the presence of the impingement edge and the consequent upstream influence to the sensitive region of the shear layer at separation allows highly coherent, large-scale vortical structures to be sustained in a manner directly analogous to the Kármán wake of a cylinder. This equivalence is addressed for quasi-laminar jets and wakes by Chomaz *et al.* (1988) and Rockwell (1990). For the present case of the impinging turbulent jet, the initially developing shear layer from the channel exit is modulated by the upstream influence arising from the jet–edge interaction. This influence may be approximated, for purposes of discussion, as a dipole-like source located near the tip of the impingement edge. It is dominated by the frequency of the large-scale vortex interaction with the edge. As a consequence, the small-scale vortical structures initially formed from the corners of the channel exit, which have a much higher frequency, develop in a much less organized, non-repetitive fashion, evident by constructing space–time distributions of vorticity. They rapidly coalesce to form the large-scale vortical structures, in a manner similar to the phenomenon on collective coalescence observed for large amplitude forcing of jets in the absence of an impingement edge (Ho & Huang 1982; Rockwell 1972).

(c) Confirmation of the concept of inviscid disturbance amplification on the turbulent background of the jet is evident by comparison of the overall form of the jet undulation and large-scale vortex development with the corresponding case of an initially laminar jet, qualitatively visualized with dye or smoke. The gross form of the jet patterns is remarkably similar, again emphasizing the importance of upstream influence or feedback in promoting the emergence of large-scale, phase-repetitive vortices.

7.2. Jet-Edge Interaction and Instantaneous Loading of Edge

The quasi-periodic pressure fluctuations on the surfaces of the edge have been related to the instantaneous velocity and vorticity fields in the vicinity of the edge. The major findings are as follows.

(a) The interaction of the large-scale vortices with the edge is more complex than the traditionally assumed case of a fully evolved vortex street impinging upon the edge. Such vortices evolve from initially elongated patches of distributed vorticity that have an essentially horizontal major axis. These elliptically shaped clusters of vorticity continue to develop as they interact with the edge, undergoing simultaneous translation and tilting, such that their major axes tend towards a nearly vertical orientation. Simultaneously, the centroid of these large-scale concentrations is increasingly displaced from the plane of symmetry of the edge. The dimensionless circulation of the large-scale clusters of vorticity, based on the centerline velocity of the channel flow and the width of the channel, is $\Gamma^* = \Gamma/\pi \bar{U}_m 2h \cong 1$.

(b) Along the surface of the edge, at a location immediately downstream of the tip, the large-scale vorticity concentration and smaller-scale concentrations of opposite sense are observed. The small-scale concentrations do not, however, arise from the classical scenario

of boundary layer eruption from the surface of the edge to form the so-called secondary vortices (Curle 1953); rather, they are simply due to partitioning of the shear layer from the opposite side of the jet by the tip of the impingement edge.

(c) The surface pressure fluctuations on either side of the edge are highly nonlinear, involving rapid changes with pressure on one surface, while simultaneously, mild changes in pressure occur along the opposite surface. This nonlinearity takes the form of higher harmonic components in the spectra of the surface pressure fluctuations. Such multiple spectral peaks are, however, not due to multiple concentrations of large-scale vortices, as observed by Lucas & Rockwell (1984) for the corresponding case of the laminar jet. Rather, they are due to the complex type of vortex pattern described in (b).

(d) This type of nonlinearity, and the associated form of the spectral distribution of the fluctuating surface pressures, is preserved over a wide range of impingement length L normalized by the nozzle half-width H. Appropriate scaling of the frequency of the surface pressure fluctuation involves fL/H, in analogy with that employed for the classical laminar-jet interactions. The importance of the impingement length scale L is due to the feedback, or upstream influence, which occurs essentially instantaneously from the impingement edge to the sensitive region of the shear layer in the vicinity of the nozzle exit. The convective time scale corresponding to development of the vortex system over distance L accounts for the variation of the absolute value of frequency f of the fundamental mode of the surface pressure and thereby development of the large-scale vortices in the jet. An important distinction relative to the laminar jet is the apparent lack of occurrence of successive stages of oscillation, which are well known to occur in accord with increasingly complex patterns of large-scale vortices immediately upstream of and at the tip of the impingement edge. Such stage-like behavior does not appear to occur for the turbulent jet; rather, the nonlinear nature of the jet–edge interaction induces the higher order harmonics.

(e) In the event that the jet–edge oscillation would occur in the presence of a resonant acoustic mode of a confined system, evaluation of the hydrodynamic integrand of the integral expressing the acoustic power reveals substantial contributions from both large- and small-scale concentrations of vorticity in the vicinity of the impingement edge. This evaluation shows that resonant acoustic modes oriented transverse to the jet–edge will produce the maximum acoustic power for a given magnitude of acoustic velocity.

7.3. Turbulence Statistics of Jet

The statistics of the jet rapidly take on an identity distinct from the turbulent boundary layer in the channel. Due to separation of flow from the exit of the channel, which is characterized by inflection points in the averaged velocity profile, rapid amplification of disturbances occurs, leading to highly correlated velocity fluctuations in the streamwise and transverse directions. As a consequence, the following statements may be made.

(a) The averaged Reynolds stresses in the initial formation region of the jet, due to formation of small-scale vortices, exceeds that of the turbulent boundary layer within the channel by a factor of five. Further downstream in the jet, the onset of large-scale vortex formation is associated with averaged values of Reynolds stress of the order of 15 times that in the channel boundary layer. Finally, in regions of local interaction of the jet with the tip of the edge, the Reynolds stress can be of the order of 40 times that of the initially turbulent boundary layer.

(b) Large values of averaged Reynolds stresses in the tip region of the edge are associated with peak values of the r.m.s velocity fluctuations. The transverse component v_{rms} exhibits peak values at the tip of the edge, while the streamwise component u_{rms} shows two peak

values located immediately downstream of the tip of the edge, one on the upper surface and the other on the lower surface.

ACKNOWLEDGEMENTS

The authors are pleased to acknowledge the partial support of the National Science Foundation under Grants No. CTS-9422432 and CTS-9803734, as well as the Office of Naval Research with Grants No. N00014-94-1-0815, P00001 and N00014-94-1-1183, NASA-Langley Research Center under Grant No. NAG-1-1885, and the Air Force Office of Scientific Research, Grant No. F49620-99-1-0011. The authors benefited from the contributions of Matthew Reiss during the experimental phase of this investigation.

REFERENCES

BAJAJ, A. K. & GARG, V. K. 1977 Linear stability of jet flows. *Journal of Applied Mechanics* **44,** 378–384.

BETCHOV, R. & CRIMINALE, W. O. 1966 Spatial instability of the inviscid jet and wake. *The Physics of Fluids* **9,** 359–362.

BLAKE, W. K. & POWELL, A. 1986 The development of contemporary views of flow-tone generation. In *Recent Advances in Aeroacoustics* (eds A. Krothapali & C. A. Smith), pp. 247–325. New York: Springer-Verlag.

BROWN, G. B. 1937*a* The vortex motion causing edge tones. *Proceedings of the Physical Society of London* **49,** 493–507.

BROWN, G. B. 1937*b* The mechanism of edge-tone production. *Proceedings of the Physical Society of London* **49,** 508–521.

CHOMAZ, J. M., HUERRE, P. & REDEKOPP, L. T. 1988 Bifurcations to local and global modes in spatially-developing flows. *Physical Review Letters* **60,** 25–28.

CHYU, C.-K. & ROCKWELL, D. 1996 Near-wake structure of an oscillating cylinder: effect of controlled Kelvin–Helmholtz vortices. *Journal of Fluid Mechanics* **322,** 21–49.

CRIGHTON, D. G. 1992 The jet-edge tone feedback cycle; linear theory for the operating stages. *Journal of Fluid Mechanics* **234,** 361–392.

CURLE, N. 1953 The mechanics of edge-tones. *Proceedings of the Royal Society of London* A **216,** 412–424.

GURSUL, I., LUSSEYRAN, D. & ROCKWELL, D. 1990 On interpretation of flow visualization of unsteady shear flows. *Experiments in Fluids* **9,** 257–266.

GURSUL, I. & ROCKWELL, D. 1991 Effect of concentration of vortices on streakline patterns. *Experiments in Fluids* **10,** 294–296.

HO, C.-M. & HUANG, L. S. 1982 Subharmonics and vortex merging in mixing layers. *Journal of Fluid Mechanics* **119,** 443–473.

HOLGER, D. K., WILSON, T. A. & BEAVERS, G. S. 1977 The fluid mechanics of the edge tone. *Journal of the Acoustical Society of America* **62,** 1116–1128.

HOLGER, D. K., WILSON, T. A. & BEAVERS, G. S. 1980 The amplitude of edgetone sound. *Journal of the Acoustical Society of America* **67,** 1507–1511.

HOURIGAN, K., WELSH, M. C., THOMPSON, M. C. & STOKES, A. N. 1990 Aerodynamic sources of acoustic resonance in a duct with baffles. *Journal of Fluids and Structures* **4,** 345–370.

HOWE, M. S. 1975 Contributions to the theory of aerodynamic sound with application to excess jet noise and the theory of the flute. *Journal of Fluid Mechanics* **71,** 625–673.

HOWE, M. S. 1980 The dissipation of sound at an edge. *Journal of Sound and Vibration* **70,** 407–411.

HOWE, M. S. 1984 On the absorption of sound by turbulence and other highly dynamic flows. *Journal of Applied Mathematics* **32,** 187–209.

HOWE, M. S. 1997 Edge, cavity and aperture tones at very low Mach numbers. *Journal of Fluid Mechanics* **330,** 61–84.

HUERRE, P. 1984 Perturbed free shear layers. *Annual Review of Fluid Mechanics* **16,** 365–424.

HUERRE, P. & MONKEWITZ, P. A. 1990 Local and global instabilities of spatially developing flows. *Annual Review of Fluid Mechanics* **22,** 473–537.

JEFFERIES, R. & ROCKWELL, D. 1996 Interactions of a vortex with an oscillating leading-edge. *AIAA Journal* **34,** 2448–2450.

JOHANSSON, J. B. & SMITH, C. R. 1983 The effects of cylindrical surface modifications on turbulent boundary layers. Report FN-3, Department of Mechanical Engineering and Mechanics, Lehigh University, Bethlehem, Pennsylvania, U.S.A.

KARAMCHETI, K., BAUER, A. B., SHIELDS, W. L., STEGEN, G. R. & WOOLLEY, J. P. 1969 Some features of an edge-tone flow field. NASA HQ Conference, Basic Aeronautical Noise Research, NASA Special Publication 207, pp. 275–304.

KAYKAYOGLU, R. & ROCKWELL, D. 1986 Unstable jet–edge interaction. Part I. Instantaneous pressure fields at single frequency. *Journal of Fluid Mechanics* **169,** 125–149.

KIM, J., MOIN, P. & MOSER, R. 1987 Turbulent statistics in fully developed channel flow at low Reynolds number. *Journal of Fluid Mechanics* **177,** 133–166.

LANDRETH, C. C. & ADRIAN, R. J. 1990 Impingement of a low Reynolds number circular jet onto a flat plate at normal incidence. *Experiments in Fluids* **9,** 74–84.

LEPICOVSKY, J. & AHUJA, K. K. 1983 some new results on edge tone oscillations in high speed subsonic jets. AIAA Paper No. 83-0665.

LIN, J.-C. & ROCKWELL, D. 1998 Cinema PIV and its application to impinging vortex systems. Article FEDSM 98-5270, *Proceedings of ASME Fluids Engineering Division Summer Meeting*, June 21–25, Washington, D.C.

LIU, Z.-C., LANDRETH, C. C., ADRIAN, R. J. & HANRATTY, T. J. 1991 High resolution measurement of turbulent structure in a channel with particle image velocimetry. *Experiments in Fluids* **10,** 301–312.

LUCAS, M. & ROCKWELL, D. 1984 Self-excited jet: upstream modulation and multiple frequencies. *Journal of Fluid Mechanics* **147,** 333–352.

MONKEWITZ, P. & HUERRE, P. 1982 Influence of the velocity ratio on the spatial instability of mixing layers. *Physics of Fluids* **24,** 1137–1143.

NIEDERSCHULTE, M. 1989 Turbulent flow through a rectangular channel. Ph.D. dissertation, Department of Theoretical and Applied Mechanics, University of Illinois at Urbana-Champaign, U.S.A.

NYBORG, W. L. 1954 Self-maintained oscillations of the jet in a jet–edge system. *Journal of the Acoustical Society of America* **26,** 174–182.

POWELL, A. 1961 On the edge tone. *Journal of the Acoustical Society of America* **33,** 395–409.

ROCKWELL, D. 1972 External excitation of planar jets. *Journal of Applied Mechanics* **39,** 883–890.

ROCKWELL, D. 1983 Oscillations of impinging shear layers. Invited Lecture, 20th Aerospace Sciences Meeting of AIAA, January, 1981, Orlando, FL; AIAA Paper 81-0047; also see *AIAA Journal* **21,** 645–664.

ROCKWELL, D. 1990 Active control of globally-unstable separated flows. *Proceedings of International Symposium of ASME FED*: *Unsteady Fluid Dynamics* Vol. 92 (eds J. A. Miller & D. P. Telionis), pp. 379–394.

ROCKWELL, D. 1998 Vortex–body interactions. Invited contribution, *Annual Review of Fluid Mechanics* **30,** 199–229.

ROCKWELL, D. & LIN, J. C. 1996 *Experimental data for computational fluid dynamic simulations of fluid oscillators*: *cavity flow*. *Vol. 1 and 2*. Fluid Mechanics Laboratories Report R01, 1996, Department of Mechanical Engineering and Mechanics, Lehigh University, Bethlehem, Pennsylvania, U.S.A.

ROCKWELL, D. & LIN, J. C. 1997 Experimental data for computational fluid dynamics simulation of fluid oscillators: jet–edge flow. Fluid Mechanics Laboratories Report R01, 1997, Department of Mechanical Engineering and Mechanics, Lehigh University, Bethlehem, Pennsylvania, U.S.A.

ROCKWELL, D., MAGNESS, C., TOWFIGHI, J., AKIN, O. & CORCORAN, T. 1993 High-image-density particle image velocimetry using laser scanning techniques. *Experiments in Fluids* **14,** 181–192.

ROCKWELL, D. & NAUDASCHER E. 1978 Review—self-sustaining oscillations of flow past cavities. *ASME Journal of Fluids Engineering* **100**, 152–165.

ROCKWELL, D. & NAUDASCHER, E. 1979 Self-sustained oscillations of impinging free-shear layers. *Annual Review of Fluid Mechanics* **11,** 67–94.

SATO, H. 1960 The stability and transition of a two-dimensional jet. *Journal of Fluid Mechanics* **7,** 53–80.

STAUBLI, T. & ROCKWELL, D. 1987 Interaction of an unstable planar jet with an oscillating leading-edge. *Journal of Fluid Mechanics* **176,** 135–167.